ISSN 0973-3302

THE JOURNAL OF ACOUSTICAL SOCIETY OF INDIA

Volume 51 Number 1 January 2024

A Quarterly Publication of the ASI
https://acoustics.org.in

The Journal of Acoustical Society of India
Volume 51 Number 1 January 2024 pp. 1-50

ASI

The Journal of Acoustical Society of India

The Refereed Journal of the Acoustical Society of India (JASI)

CHIEF EDITOR:
B. Chakraborty
CSIR-National Institute of Oceanography
Dona Paula,
Goa-403 004
Tel: +91.832.2450.318
Fax: +91.832.2450.602
E-mail: bishwajit@nio.org

ASSOCIATE SCIENTIFIC EDITOR:

A R Mohanty
Mechanical Engg. Department
Indian Institute of Technology
Kharagpur-721302, India
Tel. : +91-3222-282944
E-mail : amohantyemech.iitkgp.ernet.in

Editorial Office:
MANAGING EDITOR
Mahavir Singh

ASSISTANT EDITORS:

Yudhisther Kumar
Devraj Singh
Kirti Soni
ASI Secretariat,
C/o Acoustics and Vibration Metrology
CSIR-National Physical Laboratory
Dr. KS Krishnan Road
New Delhi 110 012
Tel: +91.11. 4560.8317
Fax: +91.11.4560.9310
E-mail: asisecretariat.india@gmail.com

The Journal of Acoustical Society of India is a refereed journal of the Acoustical Society of India **(ASI)**. The **ASI** is a non-profit national society founded in 31st July, 1971. The primary objective of the society is to advance the science of acoustics by creating an organization that is responsive to the needs of scientists and engineers concerned with acoustics problems all around the world.

Manuscripts of articles, technical notes and letter to the editor should be submitted to the Chief Editor. Copies of articles on specific topics listed above should also be submitted to the respective Associate Scientific Editor. Manuscripts are refereed by at least two referees and are reviewed by Publication Committee (all editors) before acceptance. On acceptance, revised articles with the text and figures scanned as separate files on a diskette should be submitted to the Editor by express mail. Manuscripts of articles must be prepared in strict accordance with the author instructions.

All information concerning subscription, new books, journals, conferences, etc. should be submitted to Chief Editor:

B. Chakraborty, CSIR - National Institute of Oceanography, Dona Paula, Goa-403 004,
Tel: +91.832.2450.318, Fax: +91.832.2450.602, e-mail: bishwajit@nio.org

Annual subscription price including mail postage is Rs. 2500/= for institutions, companies and libraries and Rs. 2500/= for individuals who are not **ASI** members. The Journal of Acoustical Society of India will be sent to **ASI** members free of any extra charge. Requests for specimen copies and claims for missing issues as well as address changes should be sent to the Editorial Office:

ASI Secretariat, C/o Acoustics and Vibration Metrology, CSIR-National Physical Laboratory, Dr. KS Krishnan Road, New Delhi 110 012, Tel: +91.11.4560.8317, Fax: +91.11.4560.9310, e-mail: asisecretariat.india@gmail.com

ISSN 0973-3302

Printed at Alpha Printers, WZ-35/C, Naraina, Near Ring Road, New Delhi-110028 Tel.: 9810804196. JASI is sent to ASI members free of charge.

ASI

The Journal of Acoustical Society of India

A quarterly publication of the Acoustical Society of India

Volume 51, Number 1, January 2024

ARTICLES

INFORMATION

FOREWORD

The works presented in this special issue of the Journal of Acoustical Society of India (JASI) has the underlying motivation to look for objective data and corresponding categorization problems in different domains of acoustic materials ,instrumentation and under water acoustic communication along with corresponding interdisciplinary areas, which were all presented in the 50th National Symposium on Acoustics (NSA-2023), held at Veer Surendra Sai University of Technology (VSSUT), Burla, Sambalpur, Odisha during 24-26 February 2023. This issue attempts to consolidate the materials of different interesting pieces of investigations in the diverse field carried out by different researchers across India. It may quite be possible that in spite of taking utmost care in choosing the selected and thoroughly revised versions of the manuscript, some inadvertent errors might have cropped in, or there might be certain areas of research that we may have overlooked. If so, the Guest Editors (GE) regret the same.

Recent advancements in acoustic materials have significantly impacted both material science and underwater acoustics. In material science, innovative acoustic metamaterials are being developed to manipulate sound waves in unprecedented ways, leading to applications such as noise reduction, soundproofing, and ultrasonic imaging. These metamaterials, engineered to exhibit unique properties not found in natural materials, enable precise control over acoustic wave propagation, enhancing the performance of devices ranging from medical ultrasound scanners to architectural acoustics systems. In the realm of underwater acoustics, new materials are revolutionizing sonar technology, underwater communication, and marine environmental monitoring. Advanced acoustic coatings and materials with tailored acoustic impedance are being employed to improve the detection and classification of underwater objects, reduce noise pollution, and enhance the clarity of acoustic signals in complex underwater environments. These developments are crucial for advancing maritime exploration, naval defense, and environmental conservation efforts. A systematic scientific investigation into the production, perception and analysis of the materials thus requires a multidisciplinary approach involving Basic Science and Engineering Technology.

Even if one puts aside aesthetic appreciation, the task becomes formidable. It is this task that the concept of NSA has been bringing forth since its inception in 1971 and this series of edited volumes of the Journal of Acoustical Society of India (JASI) is an attempt to bring together research works happening in this ever-expanding field across the Indian subcontinent. This issue contains six papers spanning over the three broad areas, and they are: (i) acoustic materials; (ii) signal processing related to hearing, and (iii) underwater communication. In the first article related to the acoustic materials, Negi *et al.* had provided a novel utilization route for rice straw in sound-absorbing applications by employing natural deep eutectic solvent as a pretreatment media in the fabrication process. Similarly, Sunali et al had enunciated vibration damping properties of natural rubber composites developed with waste carbonaceous fillers. Mago *et al.* had investigated vibration damping and sound insulation behaviour of recycled high-density polyethylene-aloe fibre composites. In the area of signal processing related to human hearing, Agrawal and Ramamoorthy had studied the effect of hearing loss on distortion product otoacoustic emissions in humans, and Verma et al had developed a method to derive auditory filter shapes from Psychophysical Tuning Curves. Azziz and Das had employed and presented results related to massive MIMO-OFDM technique in underwater acoustic communication.

The GE sincerely hope that serious researchers, academicians, interested personalities of this unique discipline would be benefitted from this volume.

Ganeswar Nath
—Guest Editor

Soumya Saswati Sarangi
—Co-Guest Editor

The Journal of Acoustical Society of India : Vol. 51, No. 1, 2024 (pp. 1-7)

Effect of pretreatment on the sound absorption performance of cellulosic materials

Ashutosh Negi[1,2,3], Jonty Mago[1], Sunali[1], Adepu Kiran Kumar[4], Ejaz Ahmad[5], M. Ali Haider[3] and S. Fatima[1*]

[1]Centre for Automotive Research & Tribology, Indian Institute of Technology Delhi, Hauz Khas, New Delhi-110 016, India

[2]School of Interdisciplinary Research, Indian Institute of Technology Delhi, Hauz Khas, New Delhi-110 016, India

[3]Department of Chemical Engineering, Indian Institute of Technology Delhi, New Delhi-110 016, India

[4]University of Arkansas for Medical Sciences, Little Rock, Arkansas-72212, USA

[5]Department of Chemical Engineering, Indian Institute of Technology (ISM) Dhanbad-826 004, Dhanbad, India

e-mail: fatima@iitd.ac.in

[Received: 18-01-2023; Revised: 30-07-2024; Accepted: 18-09-2024]

ABSTRACT

Agricultural residues are one of the main sources of cellulose, hemicellulose, and lignin across the globe. Notably, the transformation of cellulose, hemicellulose, and lignin into value-added products such as bio-based materials, chemicals, and fuels has been an interest among researchers to create a sustainable bio-based economy. Among the bio-based materials, the utilization of pretreated agricultural residues in noise control applications has not been explored much. The present work provides a novel utilization route for rice straw (RS) in sound-absorbing applications by employing natural deep eutectic solvent (NADES) as a pretreatment media in the fabrication process. In the first stage, the RS was pre-processed to powder form. Afterward, the powdered straw was pretreated with NADES at 140ºC for 1 hour to extract the cellulosic material. In the next stage, the obtained cellulosic pulp was washed and dried for utilization as feedstock for the fabrication of sound-absorbing material. Further, physicochemical and acoustical characterizations were performed to investigate the efficacy of the NADES pretreatment. The sound absorption coefficient (SAC) of the developed material was assessed on a two-microphone impedance tube setup according to ASTM E1050-19. The noise reduction coefficient results suggest an improvement in sound absorption (pretreated RS: 0.52 and raw RS: 0.43) of the developed material after pretreatment. Furthermore, an increase in the air gap behind the sample shows a significant improvement in SAC at lower frequencies.

1. INTRODUCTION

Agricultural residues are one of the major biorenewable resources, with an annual average global availability of more than 5200 million tons[1,2]. The major constituents of agricultural residues are cellulose, hemicellulose, and lignin. Noticeably, the share of each constituent in a particular residue varies with the crop type, geographical location, and environmental factors. Among them, cellulose has been primarily explored as a potential alternative for fabricating bio-based materials. However, due to the recalcitrance nature of agricultural residues, the separation of cellulosic fraction required a pretreatment step. In the last few decades, a range of pretreatment techniques, viz, mechanical, chemical, physicochemical, and biological, have been extensively examined by researchers across the globe[3,4]. Interestingly, chemical techniques are less time consuming and providing good efficacy in biomass pretreatment. Moreover, selecting suitable chemical pretreatment media is an important aspect of ensuring the environmental sustainability of the pretreatment process[5]. Among the list of chemical pretreatment media, natural deep eutectic solvents (NADES) are considered low-cost environmentally benign alternatives due to their biorenewable characteristics, low-cost recyclability, and nontoxicity attributes[6-8]. Pretreated agricultural residues are found to be more crystalline due to an increased share of crystalline cellulosic fraction and removal of amorphous hemicellulose and lignin constituents[4,9].

Among the bio-based materials, the utilization of agricultural residues for noise control applications has been of interest among researchers for the last few decades. The global noise control materials market is more than $14 billion and increasing rapidly due to growth in the construction industry, enhanced awareness about noise pollution, and a stringent policy framework to minimize noise exposure in residential and commercial spaces[9]. S. Kamel and C. M. Liu *et al.* have examined the performance of pretreated rice straw (RS) for fabricating biomaterials, which could be employed in a range of commercial applications[10,11]. In an innovative approach, current work investigates the effect of NADES pretreatment on sound absorption of RS. The pretreated cellulosic pulp has been utilized as feedstock to fabricate sound-absorbing material. Raw and pretreated RS were characterized using an X-ray Diffractometer (XRD), Fourier Transpose Infrared Spectroscopy (FTIR), and Scanning Electron Microscopy (SEM) to examine the effect of pretreatment. Finally, the sound absorption performance of raw and pretreated RS has been examined with a two-microphone impedance tube setup.

2. MATERIAL AND METHODS

2.1 Materials

RS was collected from the Ghaziabad district of Uttar Pradesh, India. Lactic acid and choline chloride used in pretreatment media preparation were purchased from SRL Pvt Ltd. and CDH Pvt Ltd., India, respectively. RO water was used for NADES pretreated pulp washing.

2.2 Methods

Rice Straw Pre-processing : The collected RS was washed using water to remove dirt and dust from the straw cell wall. The washed straw was dried at 105°C for 24 hours in the oven. Further, it was milled to powder form using an industrial grinder. The powdered straw was sieved at 500 microns to ensure uniformity in the following stages of sound-absorbing material development.

Natural Deep Eutectic Solvent Preparation and Pretreatment : NADES consisting of lactic acid and choline chloride was prepared as per the process mentioned by Kumar *et al.*[6,12]. Further, the pre-processed RS was pretreated for a duration of 1 hour at 140ºC.

Characterization : *X-ray Diffraction :* The changes in crystallinity of raw and pretreated RS samples were examined using an X-ray diffractometer (Rikagu, Miniflex 600). The analysis was performed at operating parameters (Voltage: 40 kV, Current: 15 mA, Chiller temperature: 20ºC) in a 2 theta scan range of 10 to 40º and scanning rate of 2º/min with step increment of 0.04 . The crystallinity index (CrI) was calculated per Equation 1[13].

$$CrI = \frac{\text{Area of crystalline peaks}}{\text{Total area}} \times 100 \quad (1)$$

Fourier Transform Infrared Spectroscopy : The variation in the functional groups after pretreatment was analyzed by FTIR spectroscopy (Thermo Scientific, Nicolet iS50FT-IR). Raw and pretreated RS samples were analyzed using attenuated total reflectance (ATR) at a scanning rate of 4 cm^{-1} and 128 scans were collected in the 4000-500 cm^{-1} wavenumber range.

Scanning Electron Microscopy : The morphology of the raw RS and pretreated RS were examined by SEM (ZEISS, EVO 18).

Normal Incidence Sound Absorption Coefficient : The normal incidence sound absorption coefficient (SAC) of the raw RS and pretreated RS samples was measured on a two-microphone impedance tube setup (Brüel & Kjær, Type 4206-T) according to ASTM E1050-19[14] (Fig. 1). The developed sound-absorbing material was placed inside a 30 mm thick 3D printed polymer cavity with natural fabric cloth (cotton, jute, etc.) covering both sides. Three samples of each material were tested. The reflection coefficient (R) (Equation 2) was determined through the transfer function (H) approach, which was further utilized for calculating SAC (Equation 3).

$$R = |R| e^{jwR} = R_r + jR_i = \frac{H - e^{-jKs}}{e^{jKs} - H} e^{2jK(l+s)} \quad (2)$$

Where H = Transfer function, K = Complex wave number, s = microphone spacing, and l = distance of sample and nearest microphone.

$$SAC\ (\alpha) = 1 - |R|^2 \quad (3)$$

Moreover, the effect of air gap (10, 20 and 30 mm) behind the sample was also investigated to examine its influence on low and high-frequency sound absorption.

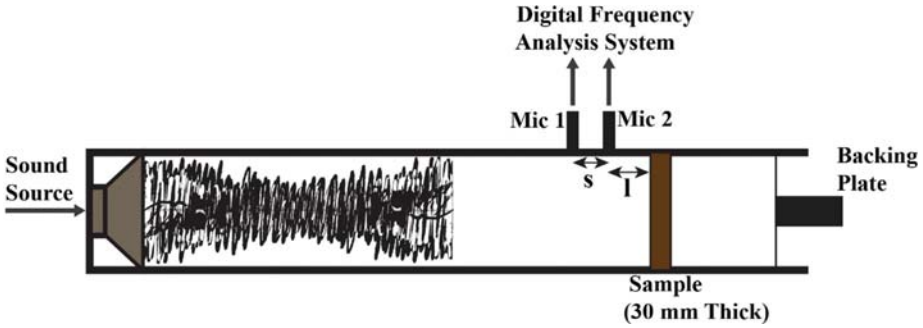

Fig. 1. Schematic of two microphone impedance tube setup.

3. RESULTS AND DISCUSSIONS

XRD pattern of NADES pretreated RS indicates an enhancement in the crystallinity compared to raw RS (Fig. 2). The increase in crystallinity of the pretreated RS can be linked to the removal/weakening of the lignin layer from the straw cell wall after pretreatment, leading to the reduction in amorphous hemicellulose and lignin content[8]. Moreover, an increase in the crystalline cellulosic fraction after pretreatment may also contribute to the increase in overall crystallinity. NADES pretreatment at 140ºC for 1 hour increases the crystallinity index of pretreated RS to 59.43% compared to 45.72% in the raw RS. He *et al.* and Kshirsagar *et al.* also observed an increase in crystallinity index after acidic and alkaline media pretreatment of rice straw[15,16].

FTIR spectrum of raw RS and pretreated RS also indicates the removal of amorphous lignin after NADES pretreatment (Fig. 3). The frequency band at 793 and 898 cm^{-1} can be linked to the C-H stretching

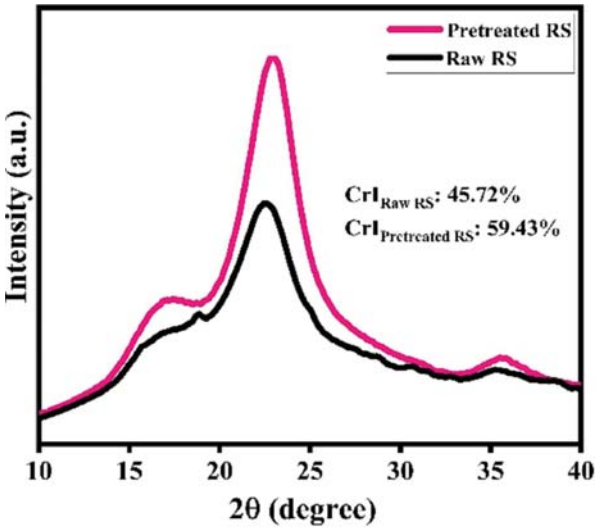

Fig. 2. XRD pattern of raw and pretreated RS.

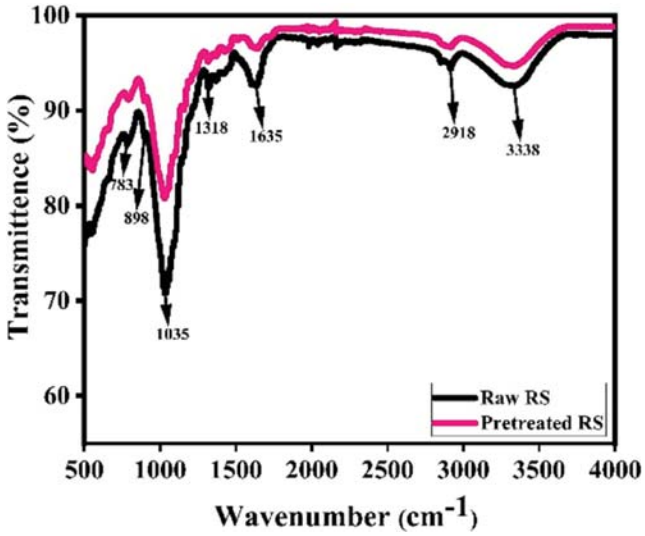

Fig. 3. FTIR spectrum of raw and pretreated RS.

of cellulose. The frequency band around 1050-1100 cm^{-1} can be assigned to the Si-O-Si functional group of silica, which is generally present in the range of 5-14% in RS[17]. The FTIR plot also indicates that the share of silica reduces in the pretreated RS.

Furthermore, the characteristic frequency bands around 1635 cm^{-1} can be assigned to the C=C stretching of lignin. A decrease in lignin content was observed in the pretreated RS, which again validates the findings of the XRD analysis. Frequency bands around 2918 cm^{-1} and 3338 cm^{-1} can be linked to C-H and O-H stretching of cellulose, respectively, showing the effect of NADES pretreatment. Other researchers have also reported similar findings[8,17].

The morphological changes in the straw cell wall were analyzed from SEM micrographs of raw RS and pretreated RS. SEM micrograph of pretreated RS indicates the formation of crakes and cavities on the straw cell wall, whereas a few minor crakes in the outer layer of raw RS are visible in the SEM micrograph (Fig. 4), which would have formed during the milling operation in a pre-processing step. Those crakes will assist in the enhancement of sound dissipation in the raw RS at a higher frequency. The SEM micrographs also indicate higher availability of the cellulosic microfibrils in the pretreated RS, ultimately enhancing its crystallinity, which has also been suggested from the XRD plot. Furthermore, the removal/weakening of the lignin layer in the pretreated RS micrograph exhibits the formation of crakes and cavities on the straw cell wall, which also supports the findings of the FTIR analysis.

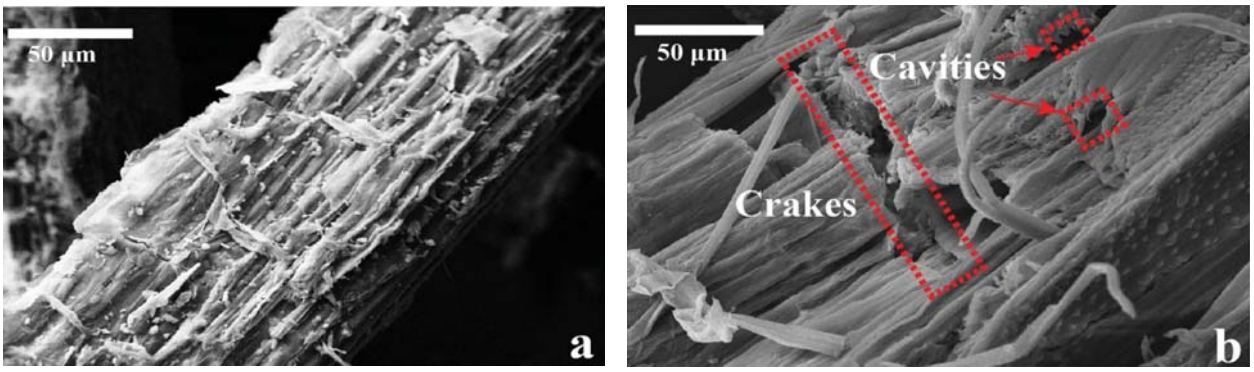

Fig. 4. SEM micrograph of (a) Raw RS and (b) Pretreated RS.

The SAC of the pretreated RS has shown significant improvement compared to raw RS (Fig. 5). Moreover, the noise reduction coefficient (NRC) was calculated (one-third octave average SAC at 250 Hz, 500 Hz, 1000 Hz, and 2000 Hz frequencies) to investigate the effect of NADES pretreatment on sound absorption[18,19]. The results indicate NRC of 0.43 and 0.52 for raw RS and pretreated RS, respectively (Table 1). The improvement in SAC of pretreated RS could be attributed to the presence of crakes and cavities in the pretreated RS compared to raw RS. Moreover, the separation of cellulosic microfibrils from the inner structure creates void spaces in the pretreated RS, which would also increase sound dissipation. Literature studies suggest that frictional and viscous losses during propagation of sound waves near crakes, cavities, and voids can be considered key contributors to the dissipation of sound energy[20].

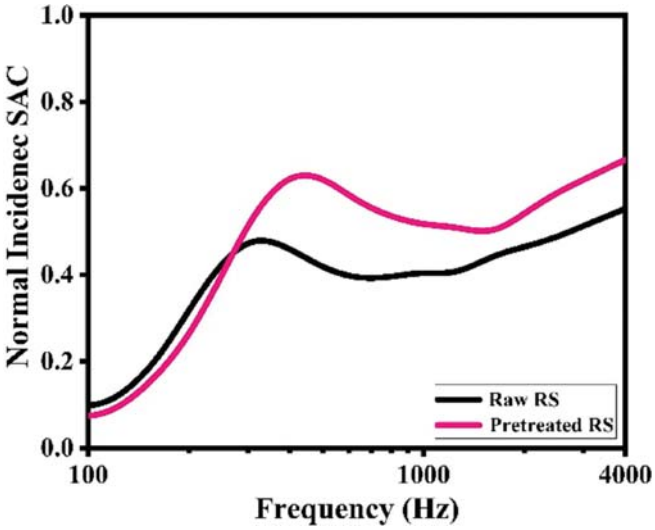

Fig. 5. SAC of raw RS and pretreatment RS.

Furthermore, the effect of the air gap behind the sample on the sound absorption of the material was also investigated. It ws observed that a 10 mm air gap increase the normal incidence SAC in raw RS (0.47 to 0.64) and pretreated RS (0.62 to 0.72) within the 500 Hz frequency range. An increase in SAC at lower frequencies can be attributed to the sound energy absorption at larger wavelengths, with the introduction of airgap behind the material[21]. This also supports the experimental findings reported by other researchers[18,19,22]. The results suggest that air gap has a distinct effect in frequencies below 500 Hz (Fig. (6) & (7)). Noticeably, a small drop in NRC (0.48 to 0.47) was evident with an increase in air gap from 20 mm to 30 mm in the raw RS case (Table 1). The reduction in NRC could be attributed to the leftward shifting of peaks which ultimately reduces the SAC at lower frequencies (Fig. 6).

M.B. Mvubu and co-workers, in their work on natural fiber-based sound-absorbing materials, have also noticed a dip in SAC after a particular air gap[21]. In the case of pretreated

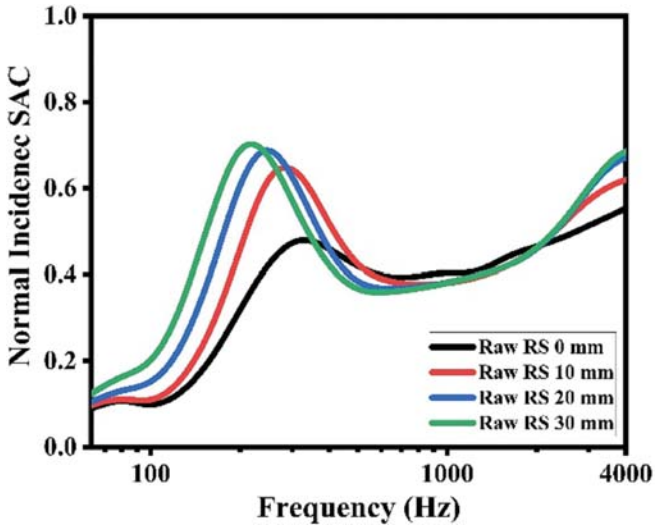

Fig. 6. Air gap effect on SAC of raw RS.

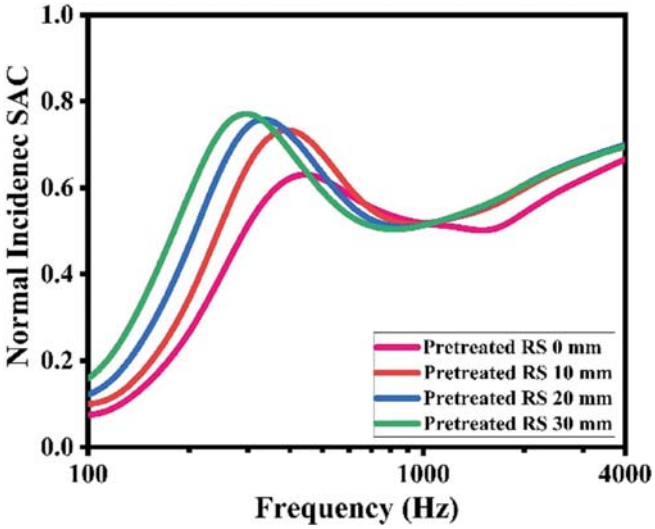

Fig. 7. Air gap effect on SAC of pretreated RS.

RS, a similar shift in peaks toward lower frequency region was also observed in (Fig. 7), resulting in a similar NRC at a 30 mm air gap (0.61) in comparison to a 20 mm air gap (0.60) (Table 1). These findings also suggest that the improvement in SAC may not be significant after a particular air gap.

Table 1. NRC of raw RS and pretreated RS.

Air gap in mm	Materials-Noise Reduction Coefficient (NRC)	
	Raw RS (30 mm)	Pretreated RS (30 mm)
0	0.43	0.52
10	0.48	0.57
20	0.48	0.60
30	0.47	0.61

4. CONCLUSION

Agricultural residues are sustainable alternatives for the fabrication of bio-based materials. Moreover, the utilization of environment-friendly pretreatment media would certainly enhance the sustainability of the sound-absorbing materials fabrication process. The key conclusions of the study are as follows:

1. The FTIR and XRD analysis indicates that NADES pretreatment removes amorphous lignin and hemicellulose and enhances the accessibility of cellulosic fraction.
2. The pretreated RS has shown improved sound absorption performance compared to raw RS. The enhancement in SAC in pretreated RS could be attributed to the presence of crakes, cavities, and voids after pretreatment. NRC results also validate the improvement in SAC after pretreatment.
3. An increase in air gap enhances sound absorption in lower frequencies. However, the improvement in SAC may not be significant after an optimal air gap. The results suggest that sound-absorbing material developed from pretreated RS can be a promising candidate for noise control applications.

5. ACKNOWLEDGMENT

Financial assistance from the Department of Science and Technology (Government of India, Grant No. DST/TDT/AGRO-52/2019) has supported this research. Furthermore, the authors would like to acknowledge characterization facilities at the Department of Chemical Engineering and Central Research Facility, Indian Institute of Technology Delhi.

6. REFERENCES

[1] Crop Images with Residue Details, Combustion Gasification & Propulsion Laboratory. (2009). http://lab.cgpl.iisc.ernet.in/ Atlas/Downloads/CropImages_with_Residue_Details (accessed January **17,** 2023).

[2] World Food and Agriculture - Statistical Yearbook 2020, FAO, 2020. DOI: 10.4060/cb1329en.

[3] Kumar A.K. and Sharma S., 2017. *Bioresour Bioprocess,* **4,** 7. DOI: 10.1186/s40643-017-0137-9.

[4] Haghighi Mood S., Hossein Golfeshan A., Tabatabaei M., Salehi Jouzani G., Najafi G.H., Gholami M., *et al.,* 2013. *Renewable and Sustainable Energy Reviews,* **27,** 77-93. DOI: 10.1016/j.rser.2013.06.033.

[5] Satlewal A., Agrawal R., Bhagia S., Sangoro J. and Ragauskas A.J., 2018. *Biotechnol Adv,* **36,** 2032-2050. DOI: 10.1016/j.biotechadv.2018.08.009.

[6] Kumar A.K., Parikh B.S. and Pravakar M., 2016. *Environmental Science and Pollution Research,* **23,** 9265-9275. DOI: 10.1007/s11356-015-4780-4.

[7] Kumar A.K., Sharma S., Shah E., Patel A., 2018. *J. Mol. Liq.,* **260,** 313-322. DOI: 10.1016/j.molliq.2018.03.107.

[8] Satlewal A., Agrawal R., Bhagia S., Das P., Ragauskas A.J., 2018. *Biofuels, Bioproducts and Biorefining,* **12,** 83-107. DOI: 10.1002/bbb.1818.

[9] Acoustic Insulation Market Size, Trends and Forecast to 2030, https://www.alliedmarketresearch.com/acoustic-insulation-market (accessed January 17, 2023).

[10] Liu C-M and Wu S-Y, 2016. *Renew Energy,* **96,** 1056-1062. DOI: 10.1016/j.renene.2015.12.059.

[11] Kamel S., 2004. *Polym Adv Technol,* **5,** 612-616. DOI: 10.1002/pat.514.

[12] Kumar A.K., Sharma S., Dixit G., Shah E., Patel A. and Boczkaj G., 2020. *Biofuels, Bioproducts and Biorefining,* **14,** 746-763. DOI: 10.1002/bbb.2110.

[13] Park S., Baker J.O., Himmel M.E., Parilla P.A. and Johnson D.K., 2010. *Biotechnol Biofuels,* **3,** 10. DOI: 10.1186/1754-6834-3-10.

[14] Standard Test Method for Impedance and Absorption of Acoustical Materials Using a Tube, Two Microphones and a Digital Frequency Analysis System, 2019. https://www.astm.org /e1050-19.html (accessed January 17, 2023).

[15] Kshirsagar S.D., Waghmare P.R., Chandrakant Loni P., Patil S.A. and Govindwar S.P., 2015. *RSC Adv,* **5,** 46525-46533. DOI: 10.1039/C5RA04430H.

[16] He Y., Pang Y., Liu Y., Li X. and Wang K., 2008. *Energy & Fuels,* **22,** 2775-2781. DOI: 10.1021/ef8000967.

[17] Chen X., Yu J., Zhang Z. and Lu C., 2011. *Carbohydr Polym,* **85,** 245-250. DOI: 10.1016/j.carbpol.2011.02.022.

[18] Raj M., Fatima S. and Tandon N., 2020. *Journal of Building Engineering,* **31,** 101395. DOI: 10.1016/j.jobe.2020.101395.

[19] Raj M., Fatima S. and Tandon N., 2020. *Applied Acoustics,* **169,** 107490. DOI: 10.1016/j.apacoust.2020.107490.

[20] Crocker M.J., 2007. Handbook of Noise and Vibration Control, 1st ed., *John Wiley & Sons, Inc., Hoboken*. DOI: 10.1002/9780470209707.

[21] Mvubu M.B., Avandia R. and Patnaik A., 2019. *J Eng Fiber Fabr,* **14,** 155892501984087. DOI: 10.1177/1558925019840874.

[22] Raj M., Fatima S. and Tandon N., 2020. *Applied Acoustics,* **159,** 107070. DOI: 10.1016/j.apacoust.2019.107070.

The Journal of Acoustical Society of India : Vol. 51, No. 1, 2024 (pp. 8-15)

Vibration damping properties of natural rubber composites developed with waste carbonaceous fillers

Sunali[1], Jonty Mago[1], Ashutosh Negi[1,2,3] and S. Fatima[1*]

[1]Centre for Automotive Research & Tribology, Indian Institute of Technology Delhi, Hauz Khas, New Delhi-110 016, India

[2]School of Interdisciplinary Research, Indian Institute of Technology Delhi, Hauz Khas, New Delhi-110 016, India

[3]Department of Chemical Engineering, Indian Institute of Technology Delhi, Hauz Khas, New Delhi-110 016, India

e-mail: fatima@iitd.ac.in

[Received: 20-01-2023; Revised: 30-07-2024; Accepted: 20-09-2024]

ABSTRACT

India generates abundant solid waste from various activities such as agriculture, industry, mining, and municipal operations, leading to severe environmental problems. Producing carbonaceous materials from these wastes through pyrolysis offers an economical, environmentally friendly, and high-recovery solution. This work focuses on fabricating natural rubber (NR) composites with carbonaceous materials, namely bamboo biochar (BBC) and recycled carbon black (RCB) as fillers. Three material configurations were fabricated: Neat NR, NR/30BBC (30 parts per hundred of rubber (phr) of BBC), and NR/30RCB (30 phr of RCB) composites. The effects of incorporating BBC and RCB into the NR matrix were evaluated through physical (ASTM D792-20), mechanical (ASTM D412-16), and vibration-damping (ASTM E756-05) properties. The vibration-damping properties were investigated in a free-layer damping (FLD) configuration using an Obrest beam setup. The results suggest that the incorporation of 30 phr of RCB to the NR matrix leads to a maximum increase in density, hardness, tensile strength (TS), and tear strength (TRS) of approximately 15.88%, 39.79%, 558.45 and 557.7%, respectively, than Neat NR. Moreover, the highest damping ratio (ξ) of 3 at the first mode of vibration was observed in NR/30RCB composites, indicating better vibration-damping properties than NR/30BBC and Neat NR.

1. INTRODUCTION

Reducing vibration transmission and isolation is critical in many engineering practices[1,2]. Active and passive methods are traditionally accepted techniques to control structural vibration. Active control methods utilize electrical devices and sensors, while passive control involves viscoelastic dampers, frictional dampers, enhancement of material damping, and joints to reduce the overall vibration levels[3]. In this context, various vibration-damping and noise-control materials have been developed by researchers to reduce structure-borne vibration and noise[4-6]. Damping refers to the dissipation of mechanical energy associated with the vibration, thereby diminishing its amplitude[7]. Recently, polymers have garnered more

attention than conventional metal materials because of their superior qualities, such as outstanding viscoelasticity, ease of mass production, lightweight nature, and good processability. Rubbers, in particular, are widely used for damping applications owing to their excellent vibration-damping capabilities, high elasticity, and strong resistance to cracking[8,9]. However, a rubber (polymer) alone may not fulfill characteristics such as strength, toughness, tear resistance, and other mechanical properties. Therefore, particulate fillers are commonly used with a polymer matrix to achieve the aforementioned properties.

Fillers are extensively used in polymer composites to enhance their physical, chemical, and mechanical properties[10]. Notably, carbonaceous materials such as carbon black (CB), carbon nanotubes, graphite, graphene, and carbon fiber are the most commonly used fillers in rubber composites. CB, in particular, has been utilized approximately 300% more than all the other fillers combined[10,11]. CB is produced through a thermal decomposition process under controlled conditions. However, this production process is energy-intensive and also contributes significantly to global CO_2 emissions[12].

Furthermore, approximately 960 million tons (Mts) of solid waste are currently generated in India annually, comprising 350 Mts of agricultural waste, 290 Mts of industrial waste, and 4.5 Mts of hazardous waste[13]. Among the agricultural wastes, a significant amount is generated from bamboo usage.

Bamboo is the grass family's most diverse group of plants with exceptional properties, such as high strength, antifungal and antibacterial attributes, natural deodorizer capabilities, and resistance to ultraviolet light[14]. As a result, approximately 4.5 Mts of bamboo are used annually in construction industries as a structural material, leading to the generation of a significant amount of waste[15].

Concurrently, according to the European Tyre Rubber Manufacturers Association (ETRMA), 289 million tires are sold annually, with approximately 1.5 billion tires ending up as waste globally. India ranks fourth in tire production, with around 74.4 million tires produced annually across 164 facilities[16]. The disposal of these waste tires poses substantial environmental and health challenges worldwide[17]. However, utilization presents an ideal strategy for managing various solid wastes, including agricultural, industrial, and municipal wastes. Hence, the current study aims to fabricate a composite material for vibration-damping applications using bamboo biochar (BBC) and recycle carbon black (RCB) as fillers in the natural rubber (NR) matrix. Additionally, this work investigates the effects of incorporating 30 parts per hundred rubber (phr) of BBC and RCB into the NR matrix on its physical, mechanical, and vibration properties. This investigation follows ASTM standards D792-20 (Density), D412-16 (Tensile Strength), D624-00 (Tear Strength), D2240-15 (Shore A Hardness), and E756-05 (Vibration Damping).

2. MATERIAL AND METHODS

2.1 Materials

NR ribbed smoked sheets (Type: RS4) and other compounding ingredients such as curing agents, plasticizers, cure accelerators, activators, and antioxidants were purchased from the local suppliers of Haryana. The carbonaceous materials, namely bamboo biochar (BBC, sourced from bamboo waste) and recycled carbon black (RCB, sourced from tire waste), were obtained from local suppliers in Delhi.

2.2 Methods

Fabrication of Composites : In this study, three composites using NR as a matrix were fabricated. The first composite was fabricated without any filler, while the other two composites were fabricated using 30 phr of BBC and 30 phr of RCB as fillers in the NR matrix. The complete formulation of fabricated composites is presented in Table 1.

The raw NR sheet was initially masticated for 5 minutes on a two-roll mill at 80°C. Subsequently, compounding ingredients such as activators and antioxidants were added and mixed with the raw NR for about 10-15 minutes at the same temperature. Thereafter, fillers and remaining compounding ingredients were mixed into the prepared masterbatch for another 10 minutes using the same two-roll mill. Finally, the masterbatch was then compression molded into sheets at a temperature of 150°C and a

Table 1. Composites formulations in phr.

Ingredients (phr)	Types of Composites		
	Neat NR	NR/30BBC	NR/30RCB
Natural Rubber (Type: RS4)	100	100	100
Bamboo Biochar (BBC)	-	30	-
Recycle Carbon Black (RCB)	-	-	30
Curing Agent	2.5	2.5	2.5
Activator 1	2.0	2.0	2.0
Activator 2	5.0	5.0	5.0
Plasticizer	10	10	10
Cure Accelerator	1.0	1.0	1.0
Antioxidant	1.5	1.5	1.5

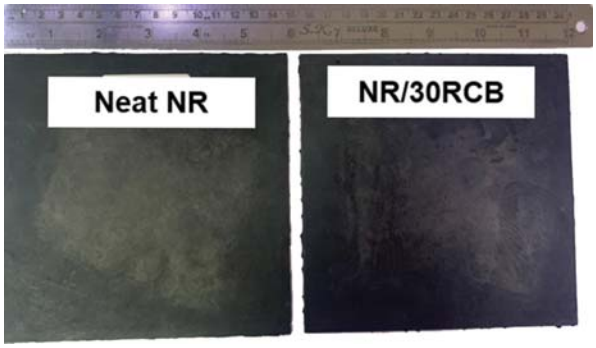

Fig. 1. Fabricated composites (Neat NR and NR/30RCB).

pressure of 1.4 MPa, with the process being held for a duration of 15 minutes. The fabricated composites are shown in (Fig. 1).

Characterization of Carbonaceous Fillers : The particle size of the BBC and RCB fillers was measured using Scanning Electron Microscopy (SEM) with a (Model: EVO50; Make: ZEISS) apparatus. The specimens for SEM were prepared using 10 mg each of BBC and RCB. Both fillers were dispersed separately through sonication for 2 hours in a 50 ml isopropanol solution, then filtered out using filter paper. The resultant specimens were gold-coated and examined under SEM at an accelerating voltage of 20 keV. Additionally, an ultimate analysis was conducted using a CHN Elemental Analyzer (Model: Vario Macro; Make: Elementer Analysensysteme Gmbh) to measure the carbon content in the BBC and RCB fillers.

Characterization of the Composites : Physical Properties : The density of fabricated Neat NR, NR/30BBC, and NR/30RCB composites was determined using an Analytical Weighing Balance (Make: Mettler Toledo; Model: ME155DU) following ASTM D792-20 standard. The specimens measuring 20 mm in length, 20 mm in width, and 2 mm in thickness were used.

Mechanical Properties : The hardness of the fabricated Neat NR, NR/30BBC, and NR/30RCB composites was tested using a Shore Hardness Meter (Make: Kori Seiki; Model: KR-12KA) as per ASTM D2240-15 standard. Cylindrical specimens with a diameter of 30 mm and a thickness of 13 mm were used for this test. The tensile strength (TS) of the fabricated composites was tested using a Universal Testing Machine (Make: Shimadzu; Model: AGS-10 kN) according to the ASTM D412-16 standard. The dumbbell-shaped specimens were prepared, and each composite was tested with five specimens at a crosshead speed of 500 mm/min at 25°C. Furthermore, the tear strength (TRS) of the fabricated composites was computed following ASTM D624-00, utilizing the results from the tensile tests.

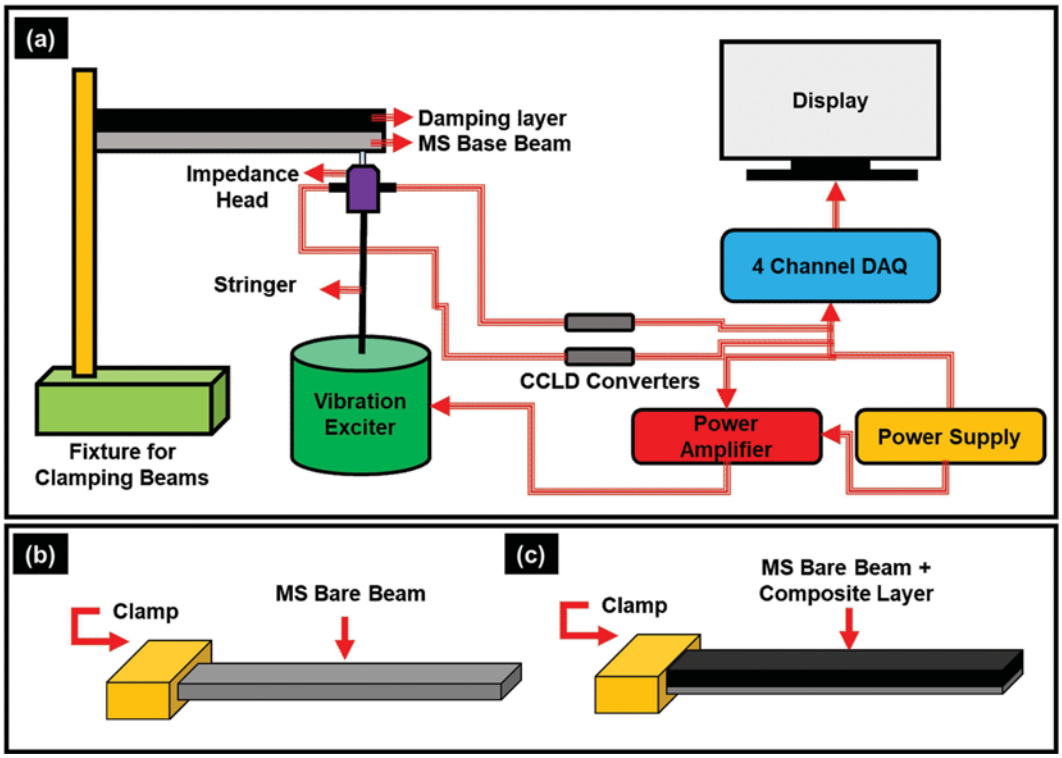

Fig. 2. Schematic of (a) Oberst beam setup for measuring vibration properties, (b) MS bare beam, and (c) MS beam + composite layer specimen.

Vibration Properties : The vibration properties (natural frequencies and damping ratios) of the fabricated Neat NR, NR/30BBC, and NR/30RCB composites were determined using an Obrest Beam setup following the ASTM E756-05 standard. The schematic of the setup is shown in (Fig. 2 (a)). The actual test setup consisted of a clamping fixture for specimens, a vibration exciter, an impedance head, a charge to delta tron (CCLD) converter, a power amplifier, and a data acquisition system. Further details about the experimental setup can be found in our previous research[5]. Four different specimen configurations were tested: (i) MS bare, (ii) MS+Neat NR layer, (iii) MS+NR/30BBC layer, and (iv) MS+ NR/30RCB layer. The specimen of the MS bare beam and MS beam with composite layer (180 mm × 10 mm × 2 mm) is illustrated in (Fig. 2 (b) & (c)). The frequency response function (FRF) measurement was conducted, and the natural frequency (ω_n) and damping ratio (ξ) were calculated using the measured FRF. Equation 1 was used to evaluate the ω_n and ξ of the tested configurations by the Half-Power Bandwidth method. Measurements were made at a constant excitation force of 0.5 N in the frequency range from 0 to 5 kHz.

$$\xi = \frac{\Delta\omega}{2\omega_n} \tag{1}$$

Where $\Delta\omega$ represents the bandwidth

3. RESULTS AND DISCUSSIONS

Carbonaceous Fillers : The SEM images of BBC and RCB carbonaceous fillers are displayed in (Fig. 3 (a) & (b)), respectively. The average particle size of BBC and RCB particles were in the range of 23.80±9.45 µm and 22.85±15.75 µm, respectively. Compared to BBC particles, the size of RCB particles was smaller. Furthermore, both fillers exhibited different shapes: the BBC particles were cylindrical, while the RCB

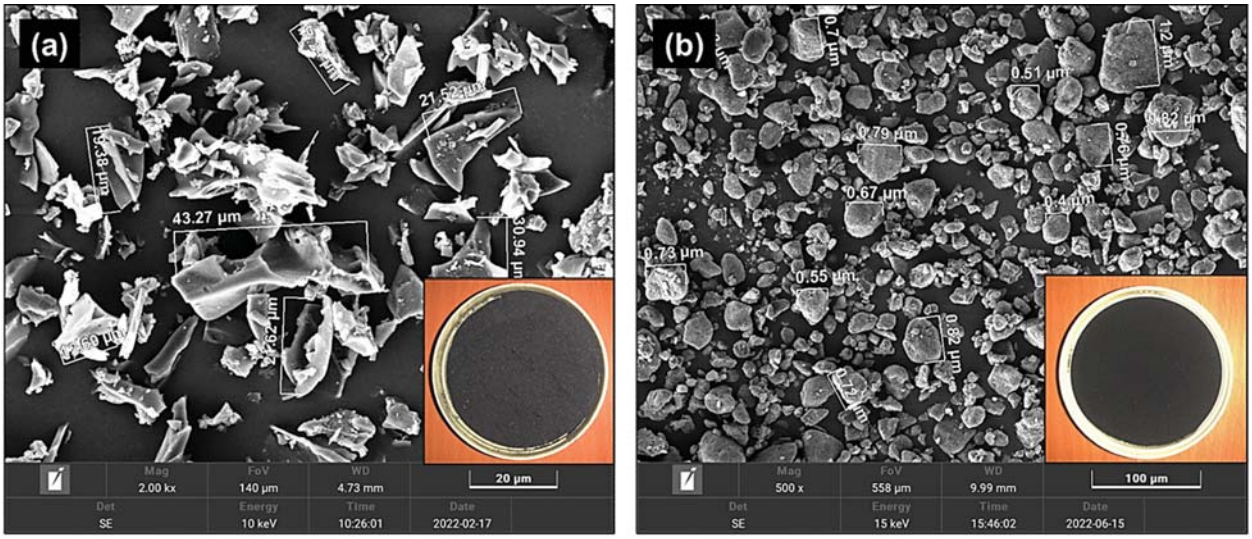

Fig. 3. SEM images of (a) BBC at 2000X and (b) RCB at 500X.

particles were spherical. The spherical shape particles contribute to the improved material-damping ability of elastomeric composites[18]. The CHNS results reveal that the BBC consists of approximately 72.2% carbon, 1.0% nitrogen, 2.1% hydrogen, 0.15% sulfur, and 24.5% oxygen, whereas the RCB sample contains approximately 79.7% carbon, 1.0% nitrogen, 0.7% hydrogen, 1.16% sulfur, and 17.5% oxygen. Therefore, the RCB filler contains a higher carbon content than the BBC filler.

NR/30BBC, and NR/30RCB composites : Density : The density values of the fabricated Neat NR, NR/30BBC, and NR/30RCB composites are shown in Table 2. The NR/30BBC and NR/30RCB composites were observed to possess higher density values than the Neat NR composite. The density value of NR/30BBC and NR/30RCB composites increased by approximately 13.23% and 15.88%, respectively, with the incorporation of BBC and RCB into the NR matrix. This increase can be attributed to the higher density of the reinforced fillers.

Table 2. Measured density values of all fabricated composites.

S No.	Type of Composite	Density (kg/m^3)
1	Neat NR	911
2	NR/30BBC	1050
3	NR/30RCB	1083

Moreover, the higher density of the NR/30RCB composite can be linked to the comparatively smaller particle size of the RCB filler, contributing to a reduction in void content within the composite.

Mechanical Properties : The results of mechanical properties, namely hardness, TS, and TRS of the Neat NR, NR/30BBC, and NR/30RCB composites, are given in Table 3. The hardness value of the

Table 3. Hardness, tensile strength, and tear strength of fabricated composites.

Types of Composite	Hardness (Shore A)	TS (MPa)	TRS (N/mm)
Neat NR	33.62±0.41	2.5±0.22	7.51±0.65
NR/30BBC	41.85±0.73	8.34 ± 0.09	25.03±0.27
NR/30RCB	47.00±0.70	16.46±1.07	49.4±3.22

fabricated composites showed an increasing trend with incorporating fillers in the polymer matrix. The NR/30RCB composites exhibited the highest hardness value than NR/30BBC and Neat NR composites, which can be attributed to the comparatively smaller particle size of RCB[19].

(Fig. 4) presents the stress versus strain curve for the Neat NR, NR/30BBC, and NR/30RCB composites under a tensile test. The results indicate that the TS of Neat NR, NR/30BBC, and NR/30RCB composites are 2.5±0.22 MPa, 8.34 0.09 MPa, and 16.46±1.07 MPa, respectively.

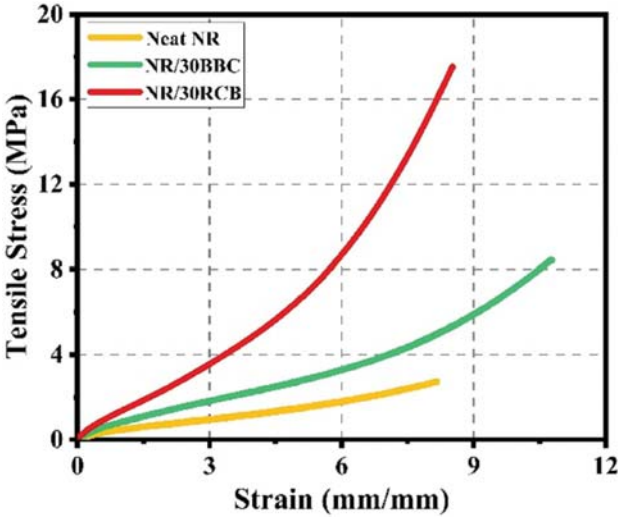

Fig. 4. Stress vs. strain curve for all fabricated composites.

The TS value of the NR/30RCB composite is approximately double that of the NR/30BBC composite. The higher carbon content, smaller particle size, and larger surface area of RCB particles contribute to a uniform dispersion in the NR matrix, enhancing the stiffness of the composite and thereby improving the TS value of the NR/30RCB composite. Additionally, incorporating filler into the NR matrix increases the TS value of the composite due to the restriction in NR chain motion[19].

Furthermore, the TRS of the composites was calculated using tensile test data. The TRS measures the resistance to crack propagation in rubber composites. As indicated in Table 3, the NR/30RCB composite demonstrates superior tear resistance than the other fabricated composites. This improvement is attributed to the high structural integrity of RCB, which enhances crack growth protection in the NR/30RCB composite. Overall, the results suggest that incorporating filler into the NR matrix improves the TRS of both NR/30BBC and NR/30RCB composites.

Table 4. ω_n's and ξ's for all measured configurations.

Specimens	Property	Mode 1	Mode 2	Mode 3	Mode 4
MS Bare	ω_n (Hz)	32.50	223.50	658.50	1317
	ξ (%)	2.90	0.40	0.20	0.22
MS+Neat NR	ω_n (Hz)	31.60	205.60	401.20	671.20
	ξ (%)	1.98	0.46	4.23	10.07
MS+NR/30BBC	ω_n (Hz)	35.00	235.50	563.50	794.00
	ξ (%)	2.30	0.89	2.01	0.66
MS+NR/30RCB	ω_n (Hz)	31.50	203.00	514.50	703.50
	ξ (%)	3.00	0.73	3.27	3.68

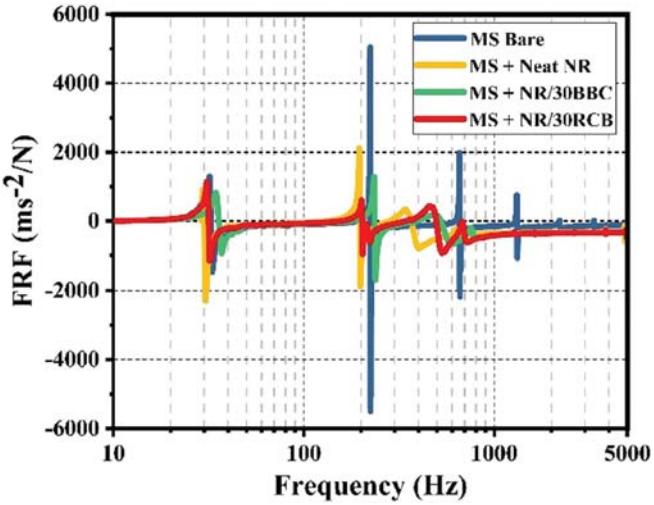

Fig. 5. FRF of all measured free layer damping configurations.

Vibration Damping : The ω_n and ξ of the tested specimens are shown in Table 4. The first four modes, which were noticed to be around 32 Hz, 220 Hz, 650 Hz, and 1300 Hz (Fig. 5), were considered for quantifying ξ's. As shown in (Fig. 5), it is evident that the θ_n's shift towards lower frequencies for the MS+Neat NR, MS+NR/30BBC, and MS+NR/30RCB configurations as than the MS bare.

Furthermore, it can also be observed that the amplitude of acceleration significantly decreases with the addition of a composite layer on the MS beam. The MS+NR/30RCB layer shows the highest ξ value at the first mode of vibration than MS+Neat NR and MS+NR/30RCB configurations. This suggests that the NR/30RCB composite is more efficient in damping than MS+NR/30BBC and MS+Neat NR composites. The large surface area and small particle size of RCB filler contribute to forming an effective stick-slip mechanism between NR chains and RCB particles, thereby enhancing the damping capability of MS+NR/30RCB composite[20].

4. CONCLUSION

Based on the above investigations, the following conclusion can be drawn:

a. Incorporating 30 phr of BBC and RCB into the NR matrix improved density values by approximately 13.23% and 15.88%, respectively, for NR/30BBC and NR/30RCB composites.

b. The NR/30BBC and NR/30RCB composites exhibited significant improvements in mechanical properties with the incorporation of BBC and RCB fillers in the NR matrix.

c. The vibration damping results indicate that the spherical shape of the RCB filler, coupled with the formation of an effective stick-slip mechanism between NR chains and RCB fillers, enhances the damping property of the NR/30RCB composites. This suggests potential applications for fabricated composites in various areas, such as vibration-damping sheets, rubber flooring, cable sheeting, and numerous small components in the automotive industry.

5. ACKNOWLEDGMENT

The authors would like to express their gratitude to the Industrial Research & Development (IRD) Unit of Indian Institute of Technology Delhi for financially supporting this Faculty Interdisciplinary Research Project (FIRP). Additionally, thanks are extended to the Department of Material Science & Engineering (DMSE) and Central Research Facility (CRF), IIT Delhi, for their assistance with the mechanical and morphological characterizations.

6. REFERENCES

[1] Sun L.L., Hansen C.H. and Doolan C., 2015. *Mech Syst Signal Process,* **50-51,** 480-497. DOI: 10.1016/j.ymssp.2014.05.008.

[2] Hasheminejad S.M. and Shabanimotlagh M., 2010. *Smart Mater Struct,* **19,** 035006. DOI: 10.1088/0964-1726/19/3/035006.

[3] Tang J. and Wang K.W., 2001. Hybrid Control, In: Encyclopedia of Vibration, *Elsevier,* pp. 649-658. DOI: 10.1006/rwvb.2001.0196.

[4] Mohanty A.R. and Fatima S., 2020. *Sound & Vibration,* **54,** 247-256. DOI: 10.32604/sv.2020.011011.

[5] Sunali, Mago J., Negi A., Pant K.K. and Fatima S., 2022. *J. Clean Prod,* **373,** 133760. DOI: 10.1016/j.jclepro.2022.133760.

[6] Fatima S. and Mohanty A.R., 2011. *Applied Acoustics,* **72,** 108-114. DOI: 10.1016/j.apacoust.2010.10.005.

[7] Chung D.D.L., 2010. *Composite Materials, Springer London,* DOI: 10.1007/978-1-84882-831-5.

[8] Kang H., Tang Y., Yao L., Yang F., Fang Q. and Hui D., 2017. *Compos B Eng,* **112,** 1-7. DOI: 10.1016/j.compositesb.2016.12.035.

[9] Wang J., Wang W., Geng X., Nishi T., Zhao X. and Zhang L., 2018. *RSC Adv,* **8,** 36172-36180. DOI: 10.1039/C8RA04644A.

[10] Song K., 2017. Micro- and nano-fillers used in the rubber industry, In: Progress in Rubber Nanocomposites, *Elsevier,* pp. 41-80. DOI: 10.1016/B978-0-08-100409-8.00002-4.

[11] Mahata D., Sarkar K., Mondal P., Prabhavale O., Dhanania S., Nando G.B. and Chattopadhyay S., 2020. *Iranian Polymer Journal,* **29,** 393-401. DOI: 10.1007/s13726-020-00803-x.

[12] Fan Y., Fowler G.D. and Zhao M., 2020. *J. Clean Prod,* 2020. **247,** 119115. DOI: 10.1016/j.jclepro.2019.119115.

[13] Pappu A., Saxena M. and Asolekar S.R., 2007. *Build Environ,* **42,** 2311-2320. DOI: 10.1016/j.buildenv.2006.04.015.

[14] Imadi S.R., Mahmood I. and Kazi A.G., 2014. Bamboo Fiber Processing, Properties, and Applications, in: Biomass Bioenergy, *Springer International Publishing, Cham,* pp. 27-46. DOI: 10.1007/978-3-319-07641-6_2.

[15] Siddiqui N., Don J., Mondal K. and Mahajan A., 2011. Environ Technol, **32,** 383-394. DOI: 10.1080/09593330.2010.501087.

[16] Williams P.T., 2013. *Waste Management,* **33,** 1714-1728. DOI: 10.1016/j.wasman.2013.05.003.

[17] Xu J., Yu J., Xu J., Sun C., He W., Huang J. and Li G., 2020. *Science of the Total Environment,* **742,** 140235. DOI: 10.1016/j.scitotenv.2020.140235.

[18] Zhang W. *et al.*, 2022. *Carbon Research,* **1,** 14. DOI: 10.1007/s44246-022-00009-1.

[19] Visakh P.M., Thomas S., Oksman K. and Mathew A.P., 2012. *Compos Part A Appl Sci Manuf,* **43,** 735-741. DOI: 10.1016/ j.compositesa.2011.12.015.

[20] Tahan Latibari S., Mehrali M., Mottahedin L., Fereidoon A. and Metselaar H.S.C., 2013. *Compos B Eng,* **50,** 354-361. DOI: 10.1016/j.compositesb.2013.02.022.

The Journal of Acoustical Society of India : Vol. 51, No. 1, 2024 (pp. 16-26)

Vibration damping and sound insulation behavior of recycled high-density polyethylene-aloe fiber composites

Jonty Mago[1], Sunali[1], Ashutosh Negi[1,2] and S. Fatima[1*]

[1]Centre for Automotive Research and Tribology, Indian Institute of Technology Delhi, Hauz Khas, New Delhi-110 016, India

[2]School of Interdisciplinary Research, Indian Institute of Technology Delhi, Hauz Khas, New Delhi-110 016, India

e-mail: fatima@iitd.ac.in

[Received: 25-01-2023; Revised: 18-04-2024; Accepted: 20-09-2024]

ABSTRACT

Nowadays, there is a significant demand for eco-friendly composites reinforced with natural fibers in various engineering sectors, including automotive, packaging, and construction. This is due to their distinctive characteristics, such as biodegradability, lightweight, and affordability. The present research attempts to fabricate the composite for vibration damping and sound insulation utilizing aloe fiber (AF) as reinforcement in recycled high-density polyethylene (rHDPE) matrix using the compression molding technique. The AF and rHDPE were in the form of a non-woven mat, and powder, respectively, was used for fabrication. Two types of materials were fabricated, *i.e.,* Neat rHDPE and rHDPE/AF/rHDPE sandwiched composite. The influence of reinforcing an AF sandwiched interlayer between rHDPE on the physical (density), mechanical (tensile strength and modulus), vibration, and acoustic properties of the composite was investigated. Vibration properties, namely natural frequencies and damping ratios of the fabricated materials, were investigated by vibration analysis with a vibration exciter, force transducer, and accelerometer according to ASTM E756-05. Further, the sound-insulating properties of fabricated materials as normal incidence sound transmission loss (STL) were measured using four microphone impedance tube setup as per ASTM E2611-19. The results suggest that the rHDPE/AF/rHDPE sandwiched composite has significantly higher vibration damping and STL compared to Neat rHDPE. An increase in vibration damping was due to vibration energy dissipation during interfacial friction between the AF-rHDPE matrix interphase of the sandwiched composite. However, improved density, stiffness, and damping of the composite with the reinforcement of the AF interlayer in the rHDPE matrix would be responsible for higher STL.

1. INTRODUCTION

Environmental noise pollution is recognized as a significant modern-day public health concern that poses a threat to both human health and the environment[1]. The World Health Organization has reported that approximately 1.1 billion young individuals worldwide, aged between 12-35 years, are susceptible to hearing loss due to noise exposure[2]. To mitigate this issue, using acoustic materials such as barriers,

insulators, and absorbers is a common and effective method[3]. Noise control with such materials is typically achieved by controlling the reflection, dissipation, and transmission when sound waves hit the material.

Notably, due to the increasing demand for acoustic materials, the global acoustic insulation market is expected to experience a compound annual growth rate (CAGR) of 3.9%, rising from $14.1 billion in 2021 to $17.1 billion by 2026[4]. Currently, polymer composites are the preferred materials for vibration damping and sound insulation due to their superior performance in vibration and noise control engineering, as they possess excellent viscoelasticity and good process capability[5]. However, these materials are synthetic and require a significant amount of oil-based resources for production, which are non-renewable and harmful to the environment and human health. Consequently, researchers are exploring using natural, recycled, and waste materials that are environmentally friendly and have a lower carbon footprint[6]. This approach has gained interest among researchers globally, who are working towards developing vibration damping and sound insulation materials that are commercially competitive, less harmful to health, and have positive environmental effects[7].

Numerous studies have been published utilizing different natural fibers (kenaf fiber, sisal fiber, banana fiber, coir fiber, flax fiber, luffa fiber, jute fiber, hemp fiber, coconut fiber, washingtonia filifera fiber, and bamboo fiber)[8-26] and wastes (farm residue- groundnut shell, wood-waste tire, waste printed circuit board, blast furnace slag, packing wastes, denim waste, rubber crumbs, automotive waste, leather cutting, Washingtonia palm tree pruning waste, and bamboo biochar)[27-38] to develop vibration-damping and sound insulation materials.

Furthermore, there is still a critical need for more investigation in the research area of utilizing natural and waste materials to fabricate vibration damping and sound-insulating materials. Thus, the proposed study investigates the utilization of recycled high-density polyethylene (rHDPE) and aloe fiber (AF) to fabricate vibration damping and sound-insulating materials using the compression molding technique. The study involves the fabrication and characterization of two types of sheets, namely Neat rHDPE and rHDPE / AF / rHDPE sandwiched composite, using a four-microphone impedance tube, a vibration exciter, a universal testing machine, and an analytical balance to determine their sound transmission loss (STL), vibration damping, tensile strength, and density respectively.

2. MATERIAL AND METHODS

2.1 Materials

In this study, recycled high-density polyethylene (rHDPE) was utilized as the matrix material, and aloe fiber (AF) was used as reinforcement for the fabrication of the composite. rHDPE was obtained from discarded shampoo bottles in the form of flakes (Fig. 1 (a)), and AF was extracted from the aloe plant; both materials were procured from the local supplier. The author's previous work explains the AF extraction process in detail[39]. Further, the obtained rHDPE flakes were pulverized into a powder form (Fig. 1 (b)) with a particle size of approximately 400$\pm$30 µm using a disc shape pulverizer, as shown in the SEM micrograph (Fig. 1 (d)).

At the same time, the extracted AF was converted into a non-woven mat of approximately 900$\pm$25 GSM (Fig. 1 (c)) through carding followed by needle punching. The average fiber diameter in a non-woven mat was measured as 24$\pm$5 µm, as shown in the SEM micrograph (Fig.1 (e)).

2.2 Methods

Fabrication of the rHDPE & rHDPE-AF Composite : Two types of materials, *i.e.,* Neat rHDPE-only rHDPE and rHDPE / AF / rHDPE sandwiched composite-one interlayer of AF between two layers of rHDPE (about 15% by weight) (Fig. 2 (a & b)), were fabricated using compression molding machine (Make: Kalson Hydromantic, Ghaziabad, India; Model: Hydraulic). The sheet with the dimensions of 280 mm × 180 mm × 6 mm at a pressure of 3$\pm$0.1 MPa and temperature of 120$\pm$5° C was fabricated. The heating rate was kept at 1°C / min and three degassing cycles were applied during the molding. The sheet was cooled

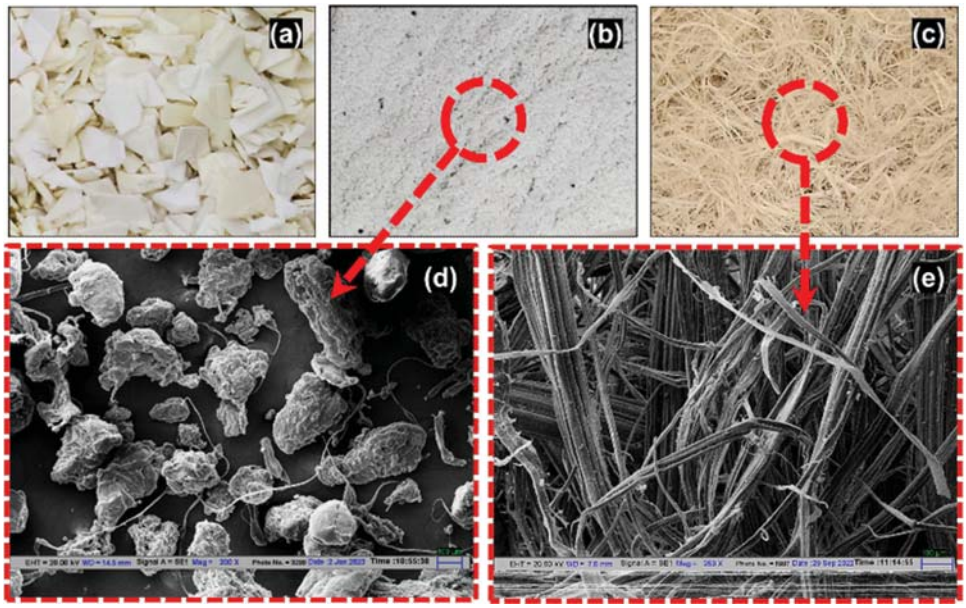

Fig. 1. Pictures of (a) rHDPE flakes, (b) rHDPE powder, and (c) aloe fiber; SEM micrograph of (d) rHDPE powder and (e) aloe fiber.

Fig. 2. (a) Type 1-Neat rHDPE (b) Type 2-rHDPE/AF/rHDPE sandwiched composite.

naturally inside the mold under the applied pressure. Further, from both the Neat rHDPE and rHDPE/AF/rHDPE sandwiched composite fabricated sheets, the multiple specimens for physical, mechanical, vibration, and acoustic characterizations were produced using a water jet cutting machine (Make: Omax, USA; Model: Protomax).

Characterization of rHDPE & rHDPE-AF Composite : Physical Properties : ASTM D792-20[40] test method B was used to measure the Neat rHDPE and rHDPE/AF/rHDPE sandwiched composite density following Archimedes principle. The measurement was performed on the Analytical Weighing Balance (Make: Mettler Toledo, Switzerland; Model: ME155DU) at 23±2°C. The ethanol, with a density of 789 kg/m^3, was used as the test liquid in this study. The weighing balance has calculated the density using Equation 1[41].

$$\rho_m = \frac{\rho_e \times W_a}{W_a - W_e} \quad (1)$$

Where ρ_m (kg/m^3) = density of test material (Neat rHDPE and rHDPE/AF/rHDPE sandwiched composite), ρ_e (kg/m^3) = density of the ethanol, w_a (g) = weight of the test material in the air, and w_e (g) = weight of the test material in the ethanol.

Mechanical Properties : ASTM 638-14[42] standard was followed to test the tensile properties of the Neat rHDPE, and rHDPE/AF/rHDPE sandwiched composite. Type I-shape specimens, as per ASTM 638-14, were used for the tensile testing. The testing was done on the Universal Testing Machine (Make: Zwick/

Roell, Germany; Model: Z010). The specimens were held in place using pneumatic jaws and tested at a crosshead speed of 50 mm/min. The test results were recorded in terms of the load applied and the deformation observed. Further, the tensile stress (σ) in MPa, strain (ε) in mm/mm, and tensile modulus (E) in GPa were calculated with Equations 2, 3, and 4[43]. The average values for tensile strength (TS), modulus (TM), and elongation at break (EB) were reported based on three measurements.

$$\sigma = \frac{F}{bd} \tag{2}$$

$$\varepsilon = \frac{\Delta L}{L_0} \tag{3}$$

$$E = \frac{\sigma}{\varepsilon} \tag{4}$$

Where F (N) = tensile load, b (mm) = width of the specimen's narrow section (13 mm), d (mm) = specimen's thickness (6 mm), L_o (mm) = specimen's gage length (50 mm) and ΔL (mm) = change in length under load.

Vibrational Properties : ASTM E0756-05[44] standard was followed to evaluate the natural frequencies and damping ratios of the rHDPE and rHDPE/AF/rHDPE sandwiched composite. The beam specimens of 180 mm length, 10 mm width, and 6 mm thickness were used for the vibration damping testing. Specimens were tested in clamped boundary conditions as a cantilever beam configuration (one end clamped and one end free). (Fig. 3) shows the schematic view of the vibration testing setup. A vibration exciter (Make: B&K, Denmark; Model: Type 4809;) was used to apply the exciting force. The applied force and vibration response were measured using a stringer with the impedance head (Make: B&K, Denmark; Model: Type 8001) mounted on the vibration exciter. The power amplifier (Make: B&K, Denmark; Model: Type 2270) was used to amplify the voltage signal generated through the data acquisition system (Make: B&K, Denmark; Model: Type 3160-A-042). The charge to deltatron convertor (CCLD) (Make: B&K, Denmark; Model: Type 2647-B) connectors were used to convert the charge signal to the voltage signal. The data acquisition system has recorded and converted all the data into a digital form. In the present work, the constant excitation force of 0.25 N was applied in the middle of the beam specimen. Vibration response was measured in the frequency range of 0-1.6 kHz at a resolution of 0.25 Hz (6400 FFT lines). The frequency response function (FRF) plot was generated from the recorded force and vibration data through data processing in the BK connect software. The first four natural frequencies and damping ratios of the rHDPE and rHDPE/AF/rHDPE sandwiched composite were extracted from the FRF plot using the half-power bandwidth method (Equation 5)[9]. The vibration-damping testing was repeated five times for each material. The results of the best of the five signals were reported.

$$\varsigma = \frac{\Delta\omega}{2\omega_n} \tag{5}$$

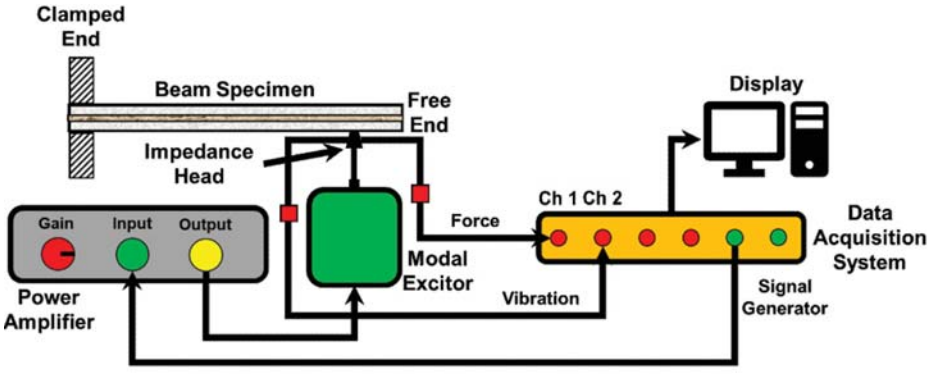

Fig. 3. Schematic view of test setup for vibration testing.

Where ζ = damping ratio, $\Delta\omega$ (Hz) = bandwidth and ω_n (Hz) = natural frequency

Acoustical Properties : ASTM E2611-19[45] standard-based four microphone impedance tube setup (Make: B&K, Denmark; Model: Type 4206-T) was employed to evaluate the normal incidence sound transmission loss (STL) of the rHDPE, and rHDPE/AF/rHDPE sandwiched composite. Four microphone impedance tube setup was used in the present study comprised of the following components : 100 mm and 29 mm diameter tube equipped with an inbuilt speaker for random noise signal generation, four-quarter inch phase-matched microphones for noise signal measurement (Make: B&K, Denmark; Model: Type 4187), a preamplifier (Make: B&K, Denmark; Model: Type 2670) for the amplifying microphone output signal, a power amplifier (Make: B&K, Denmark; Model: Type 2735) for amplifying the output signal of the speaker, Lan XI data acquisition system (Make: B&K, Denmark; Model: Type 3160-A-042) with a front end (Make: B&K, Denmark; Model: Type UA-2102-042), having four channel input for microphone data recording and one channel output for generating the random noise signal. The four-microphone impedance tube setup schematic is illustrated in (Fig. 4). Theoretically, sound transmission is defined as the "logarithmic ratio of sound energy transmitted through the material to the incidence sound energy on the material." Mathematically, it can be given as Equation 6. In the present work, the measurement was performed using the transfer matrix method, which involves measurement on two load conditions (rigid and anechoic termination). Test specimens of 100 mm and 29 mm diameter were used for the STL measurement within the frequency ranges of 63 Hz-1.6 kHz and 500 Hz to 6.4 kHz, respectively. These measurements were conducted in a controlled environment of 24°C and 50% relative humidity. During the testing, the specimens were centrally positioned in the impedance tube using ring-type holders. Three repetitions were performed for each diameter specimen, and an average normal incidence STL was reported.

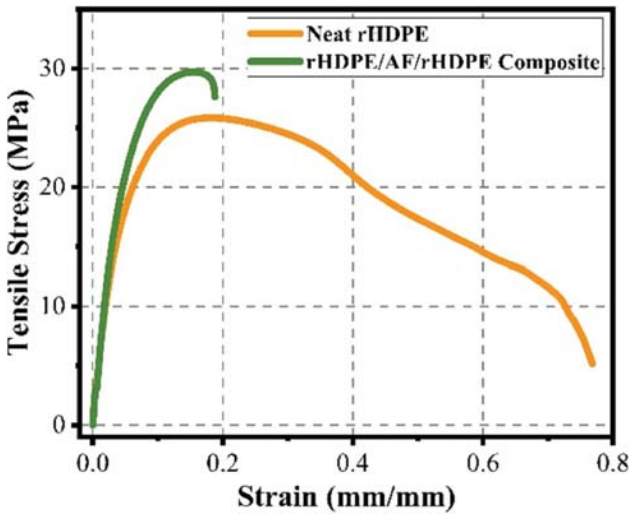

Fig. 4. Schematic view of four microphone impedance tube setup for normal incidence STL.

$$STL = 10 \log_{10}\left(\frac{W_i}{W_t}\right) = 10 \log_{10}\left(\frac{1}{\tau}\right) \quad (6)$$

Where STL (dB) = sound transmission loss, W_i (W) = incident sound power, W_t (W) = transmitted sound power, $\tau = \frac{W_t}{W_i}$ = power transmission coefficient.

3. RESULTS AND DISCUSSIONS

Density : The obtained density values for the fabricated and procured materials are tabulated in Table 1. The result reveals that the density of the rHDPE/AF/rHDPE sandwiched composite (987 kg/m^3) was approximately 1.34% higher compared to (overall 4% higher compared to rHDPE flakes) that of the Neat rHDPE (974 kg/m^3). The increase in density was primarily due to the reinforcement of the higher-density AF (1303 kg/m^3) interlayer. However, approximately a 2.63% increase in density was observed when rHDPE flakes (949 kg/m^3) were converted into a Neat rHDPE sheet (975 kg/m^3) through compression molding. The reason for the higher density of the compressed Neat rHDPE is the compression molding process. During compression molding, the flakes are heated and then compressed under high pressure

Table 1. Density values of procured and fabricated materials.

Material Name	Density (kg/m^3)
rHDPE Flakes	949
AF	1303[39]
Neat rHDPE sheet	974
rHDPE/AF/rHDPE Sandwiched Composite Sheet	987

in a mold. This process causes the flakes to melt and flow, filling voids and creating a more homogenous and compact material[46,47].

Tensile Strength and Modulus : The stress versus strain plot of Neat rHDPE and rHDPE / AF / rHDPE sandwiched composite are shown in (Fig. 5). Table 2 presents the calculated results of the tensile properties (TS, TM, and EB) of Neat rHDPE and rHDPE / AF / rHDPE sandwiched composite. Generally, for the fiber-reinforced polymer composite, the TS measures the strength of the interfacial adhesion between the fiber and the matrix. Whereas TM depends on various factors, such as the fiber content, aspect ratio, and wettability of the fiber within the matrix[43]. In the present study, the rHDPE / AF / rHDPE sandwiched composite demonstrated a steep increase in the slope of the stress versus strain plot, indicating a higher TS, which was increased by approximately 14.06% with the reinforcement of the AF interlayer between two layers of the rHDPE matrix. Furthermore, the rHDPE / AF / rHDPE sandwiched composite displayed a 22.58% enhancement in the TM (stiffness) compared to the Neat rHDPE. The improvement in TS and TM can be attributed to the fact that the reinforcement of fibers in the polymer matrix increases the load-bearing capacity of the composite[48,49]. However, it was observed that the ductility of the rHDPE matrix was negatively impacted by the reinforcement of the AF interlayer, as evidenced by a 79.62% decrease in the EB. Moreover, the results obtained in the present work are comparable with the tensile properties of flax and cotton fiber fabric blends-recycled polyethylene composites studied by Foulk *et al.*[50].

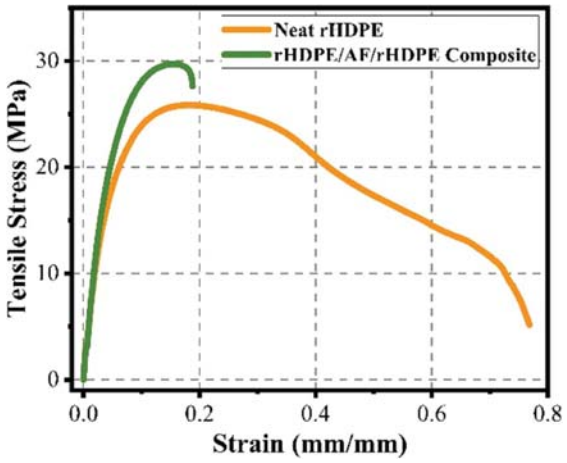

Fig. 5. Tensile stress versus strain plot for the Neat rHDPE and rHDPE / AF / rHDPE sandwiched composite.

Table 2. Tensile properties of the neat rHDPE and rHDPE/AF/rHDPE sandwiched composite.

Parameter	Neat rHDPE	rHDPE/AF/rHDPE Sandwiched Composite	% Change
Tensile Strength (MPa)	26.10±0.45	29.77±0.44	+14.06
Tensile Modulus (GPa)	0.62±1.60	0.76±0.02	+22.58
Elongation at Break (mm)	42.40±3.48	8.64±0.54	-79.62

Natural Frequency and Damping Ratio : (Fig. 6) display FRF plot for Neat HDPE and rHDPE/AF/rHDPE sandwiched composite for 10 to 1600 Hz frequency range. The four peaks in the FRF plot correspond to natural frequencies; those were considered for evaluating the damping ratios, as tabulated in Table 3. (Fig. 6) exhibits that the natural frequencies for all vibration modes were higher for rHDPE/AF/rHDPE composite compared to Neat rHDPE. The shift in natural frequencies of the rHDPE/AF/rHDPE sandwiched composite towards the higher side can be attributed to the increase in the stiffness (approximately 22.58% increase in TM) of the composite with the reinforcement of an AF interlayer within the rHDPE matrix. Furthermore, the results indicate that the rHDPE/AF/rHDPE sandwiched composite showed a higher damping ratio in the first and second vibration modes. This suggests that the rHDPE/AF/rHDPE sandwiched composite has superior damping capabilities compared to Neat rHDPE. Also, it can be observed from (Fig. 6) that the amplitude of vibration for the rHDPE/AF/rHDPE sandwiched composite was significantly lower compared to Neat rHDPE. Moreover, the most significant damping effect was observed in rHDPE/AF/rHDPE sandwiched composite at the second vibration mode (Neat rHDPE-0.37 & rHDPE/AF/rHDPE composite-2.62). The dissipation of vibrational energy in fiber-reinforced polymer composite can be achieved through the viscoelastic nature of the polymer matrix and the damping at the interphase, specifically through the dissipation of vibration energy due to interfacial friction between the fiber and polymer interphase[51,52]. Reinforcing an interlayer of AF within the rHDPE matrix enhances the dissipation of vibrational energy through the generation of interfacial friction between the AF and the surrounding rHDPE matrix, as well as through the viscoelastic properties of the rHDPE matrix. As a result, the rHDPE/AF/rHDPE composite demonstrates higher damping compared to Neat rHDPE.

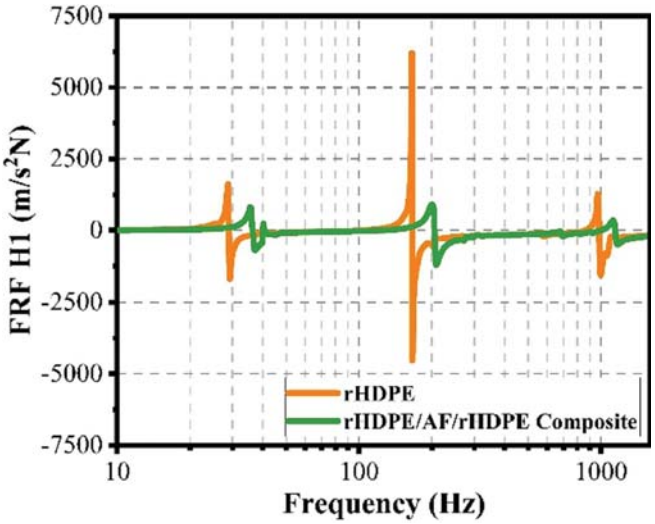

Fig. 6. FRF plot for the Neat rHDPE and rHDPE/AF/rHDPE sandwiched composite for 10 to 1600 Hz frequency range.

Table 3. Natural frequencies and damping ratios of Neat rHDPE and rHDPE/AF/rHDPE sandwiched composite.

Mode	Neat rHDPE		rHDPE/AF/rHDPE Composite	
	ω_n (Hz)	ζ (%)	ω_n (Hz)	ζ (%)
1	29	1.445	37	1.458
2	166	0.37	207.25	2.62
3	577.5	2.578	692.75	2.265
4	986.5	1.454	1146	1.041

Sound Transmission Loss : (Fig. 7) shows the normal incidence STL plot for Neat rHDPE and rHDPE/AF/rHDPE sandwiched composite over a frequency range of 63 to 5000 Hz. Both plots demonstrate a similar pattern, indicating that STL is a frequency-dependent phenomenon that can be divided into four distinct regions based on the underlying physical mechanisms: (1) The stiffness-controlled region at lower frequencies, where the STL is dependent on the material's and mounting's stiffness, (2) The resonance-controlled region at lower-medium frequencies, where the STL is dependent on the material damping properties, (3) The mass-controlled region at medium-higher frequencies, where the STL is dependent on the material surface density, and (4) The coincidence-controlled region at higher frequencies, where the STL is dependent on the material's bending stiffness[53-55]. For both materials, the frequency ranges for these regions are identified as follows: 63-100 Hz for the stiffness-controlled region, 125-1000 Hz for the resonance-controlled region, 1250-2000 Hz for the mass-controlled region, and above 2500 Hz for the coincidence-controlled region. The rHDPE/AF/rHDPE sandwiched composite exhibited a higher STL compared to the Neat rHDPE across all frequencies. Both sheets showed the highest STL (70.57 and 74.38 dB) in the 2000 Hz octave frequency band. The average STL of Neat rHDPE was 56.42 dB. In comparison, the reinforcement of AF in the rHDPE matrix resulted in a slight improvement of approximately 5.94% (59.77 dB) in sound insulation properties. The superior sound insulation properties of the rHDPE/AF/rHDPE sandwiched composite can be attributed to its higher surface density (Neat rHDPE-5.84 kg/m^2 and rHDPE/AF/rHDPE sandwiched composite-5.92 kg/m^2), tensile modulus, i.e., stiffness (Neat rHDPE-0.62 GPa and rHDPE/AF/rHDPE sandwiched composite-0.76 GPa), and vibration damping, *i.e.,* damping ratio (Neat rHDPE-0.37 and rHDPE/AF/rHDPE sandwiched composite-2.62 at the second vibration mode).

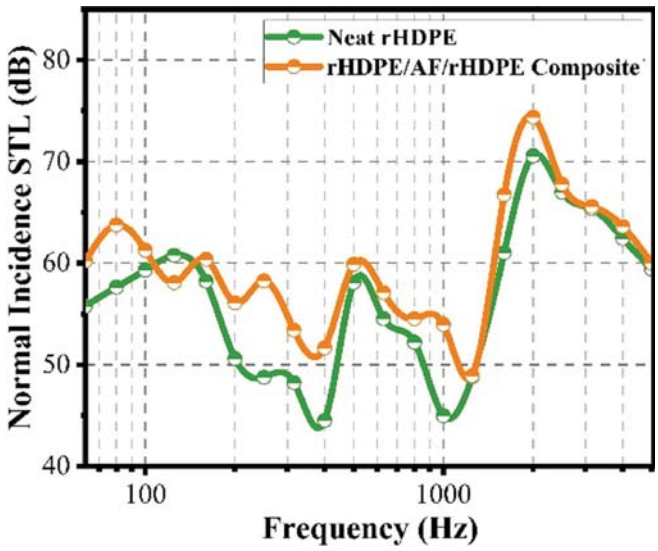

Fig. 7. Normal incidence STL plot of the Neat rHDPE and rHDPE/AF/rHDPE sandwiched composite for the frequency range of 63 to 5000 Hz.

4. CONCLUSION

Based on the studies conducted on the Neat rHDPE and rHDPE/AF/rHDPE sandwiched composite, the following conclusions could be drawn:

1. Reinforcing a higher-density AF interlayer in rHDPE/AF/rHDPE sandwiched composite led to an approximately 1.34% increase in density. In comparison, compression molding of rHDPE flakes into a Neat rHDPE sheet increased its density by approximately 2.63%. The increase in density was due to the filling of voids and the fabrication of more homogenous and compact material.

2. The tensile properties (TS, TM, and EB) of rHDPE and rHDPE/AF/rHDPE sandwiched composite were investigated. It was found that the reinforcement of the AF interlayer increased the TS by approximately 14.06% and TM by 22.58%. The improvement in TS and TM can be attributed to the increased load-bearing capacity of the composite due to the reinforcement of fibers. However, the ductility of the rHDPE matrix decreased by approximately 79.62% with the reinforcement of the AF interlayer.
3. The rHDPE/AF/rHDPE sandwiched composite showed higher natural frequencies and damping ratios compared to Neat rHDPE. The increase in stiffness and dissipation of vibrational energy due to interfacial friction between the interlayer of the AF-rHDPE matrix interphase contributed to the superior damping capabilities of the composite. Additionally, the amplitude of vibration for the rHDPE/AF/rHDPE sandwiched composite was significantly lower compared to Neat rHDPE.
4. The rHDPE/AF/rHDPE sandwiched composite showed a higher STL compared to the Neat rHDPE across all frequencies, with an approximately 5.94% improvement in sound insulation properties. This improvement can be attributed to the composite's higher surface density, tensile modulus (stiffness), and vibration damping.

5. FUNDING

The authors wish to express their gratitude to the Department of Science and Technology (DST), India, for their financial support in setting up the impedance tube as part of the project titled "Sustainable Processing of Agro-residual Waste to Produce Acoustic Materials and Bio-renewable Chemicals using Green Solvents" [Grant No. DST/TDT/AGRO-52/2019] Additionally, thanks are extended to the Faculty Interdisciplinary Research Project by the Industrial Research and Development Unit of the Indian Institute of Technology Delhi for their financial contribution to the project, "Development of Vibration and Sound Dampening Materials from Biochar Obtained from Waste Lignocellulosic Biomass" [Project No.: MI02077].

6. REFERENCES

[1] Goines L. and Hagler L., 2007. *South Med J,* **00,** 287-294. DOI: 10.1097/SMJ.0b013e3180318be5.

[2] WHO releases new standard to tackle rising threat of hearing loss, 2022. https://www.who.int/news/item/02-03-2022-who-releases-new-standard-to-tackle-rising-threat-of-hearing-loss (accessed February 22, 2023).

[3] Rajappan S., Bhaskaran P. and Ravindran P., 2017. *Journal of Applied Sciences.* **17,** 339-356. DOI: 10.3923/jas.2017.339.356.

[4] Acoustic Insulation Market, Industry Size Forecast, 2023. https://www.marketsandmarkets.com/Market-Reports/acoustic-insulation-market-41399747.html (accessed February 22, 2023).

[5] Patnaik A., Mvubu M., Muniyasamy S., Botha A. and Anandjiwala R.D., 2015. *Energy Build,* **92,** 161-169. DOI: 10.1016/j.enbuild.2015.01.056.

[6] Asdrubali F., D'Alessandro F. and Schiavoni S., 2015. *Sustainable Materials and Technologies,* **4,** 1-17. DOI: 10.1016/j.susmat.2015.05.002.

[7] la Mantia F.P. and Morreale M., 2011. *Compos Part A Appl Sci Manuf,* **42,** 579-588. DOI: 10.1016/j.compositesa.2011.01.017.

[8] Hao A., Zhao H. and Chen J.Y., 2013. *Compos B Eng,* **54,** 44-51. DOI: 10.1016/j.compositesb.2013.04.065.

[9] Munde Y.S., Ingle R.B. and Siva I., 2019. *Noise & Vibration Worldwide,* **50,** 13-21. DOI: 10.1177/0957456518812784.

[10] Singh V.K. and Mukhopadhyay S., 2022. *Journal of Industrial Textiles,* **51,** 1355-1375. DOI: 10.1177/1528083720901823.

[11] Manral A. and Bajpai P.K., 2022. Proceedings of the Institution of Mechanical Engineers, Part L: *Journal of Materials: Design and Applications,* **236,** 2467-2479. DOI: 10.1177/14644207221094205.

[12] Singh V.K. and Mukhopadhyay S., 2022. *Journal of Natural Fibers,* **19,** 349-358. DOI: 10.1080/15440478.2020.1745116.

[13] Haris A., Kureemun U., Tran L.Q.N. and Lee H.P., 2019. *Advanced Composite Materials,* **28,** 335-346. DOI: 10.1080/09243046.2018.1533347.

[14] Huang K., Tran L.Q.N., Kureemun U., Teo W.S. and Lee H.P., 2019. *Journal of Natural Fibers,* **16,** 729-743. DOI: 10.1080/15440478.2018.1433096.

[15] Koruk H., Ozcan A.C., Genc G. and Sanliturk K.Y., 2021. *Journal of Natural Fibers,* **19,** 6239-6254. DOI: 10.1080/15440478.2021.1907832.

[16] Koruk H., Ozcan A.C., Genc G. and Koruk H., *Journal of Natural Fibers,* **19,** 1217-1225. DOI: 10.1080/15440478.2020.1764446.

[17] Thakare P.A., Kumar N. and Ugale V.B., 2019. *Mater Today Proc,* **19,** 686-690. DOI: 10.1016/j.matpr.2019.07.754.

[18] Koruk H. and Genc G., 2015. *Mater Lett,* **157,** 166-168. DOI: 10.1016/j.matlet.2015.05.071.

[19] Dragonetti R., Napolitano M., Boccarusso L. and Durante M., 2020. *Applied Acoustics,* **167,** 107379. DOI: 10.1016/j.apacoust.2020.107379.

[20] Fatima S. and Mohanty A.R., 2011. *Applied Acoustics,* **72,** 108-114. DOI: 10.1016/j.apacoust.2010.10.005.

[21] Wan Mamat Ali W., Ooi L.E. and Thirmizir M.Z.A., 2020. *IOP Conf Ser Mater Sci Eng,* **815,** 012004. DOI: 10.1088/1757-899X/815/1/012004.

[22] Takagi H., Mori H. and Nakaoka M., 2015. In: *Materials Characterisation,* **VII,** pp. 243-249. DOI: 10.2495/MC150221.

[23] Djamel Edinne G., Ramdane Y., Nouredine O. and Nadir B., 2022. *Journal of Vibroengineering,* **24,** 1502-1511. DOI: 10.21595/jve.2022.22847.

[24] di Landro L. and Lorenzi W., 2009. *J Biobased Mater Bioenergy,* **3,** 238-244. DOI: 10.1166/jbmb.2009.1030.

[25] Gelfuso M.V., Thomazini D., Souza J.C.S. de and Lima Junior J.J. de, 2013. Materials Research, **17,** 367-372. DOI: 10.1590/S1516-14392013005000200.

[26] Etaati A., Mehdizadeh S.A., Wang H. and Pather S., 2014. *Journal of Reinforced Plastics and Composites,* **33,** 330-341. DOI: 10.1177/0731684413512228.

[27] Sampathrajan A., Vijayaraghavan N.C. and Swaminathan K.R., 1991. *Bioresour Technol,* **35,** 67-71. DOI: 10.1016/0960-8524(91)90083-V.

[28] Zhao J., Wang X-M, Chang J.M. Chang, Yao Y. and Cui Q., 2010. *Compos Sci Technol,* **70,** 2033-2038. DOI: 10.1016/j.compscitech.2010.03.015.

[29] Cai J., Fu Q., Long M., Liao G. and Xu Z., 2017. *Compos Sci Technol,* **145,** 132-137. DOI: 10.1016/j.compscitech.2017.03.043.

[30] Hung T.C., Huang J.S., Wang Y.W. and Lin K.Y., 2014. *Constr Build Mater,* **50,** 328-334. DOI: 10.1016/j.conbuildmat.2013.09.042.

[31] Islam S., el Messiry M., Sikdar P.P., Seylar J. and Bhat G., 2022. *Journal of Industrial Textiles,* **51,** 6001S-6027S. DOI: 10.1177/1528083720940746.

[32] Sezgin H., Kucukali-Ozturk M., Berkalp O.B. and Yalcin-Enis I., 2021. *J Clean Prod,* **304,** 127132. DOI: 10.1016/j.jclepro.2021.127132.

[33] el Messiry M. and Ayman Y., 2021. *Journal of Industrial Textiles,* **51,** 5347S-5369S. DOI: 10.1177/15280837211039574.

[34] Can Y., 2019. *Acta Phys Pol A,* **135,** 772-774. DOI: 10.12693/APhysPolA.135.772.

[35] Barbanera M., Belloni E., Buratti C., Calabrò G., Marconi M., Merli F. and Armentano I., 2020. *J Mater Cycles Waste Manag,* **22,** 1339-1351. DOI: 10.1007/s10163-020-01024-3.

[36] Ferrández-García C.C., Ferrández-García C.E., Ferrández-Villena M., Ferrández-García M.T. and García-Ortuño T., 2017. *Bioresources,* **12,** 8047-8057. DOI: 10.15376/biores.12.4.8047-8057.

[37] Sunali, Mago J., Negi A., Pant K.K. and Fatima S., 2022. *J Clean Prod,* **373,** 133760. DOI: 10.1016/j.jclepro.2022.133760.

[38] Sunali, Mago J., Negi A. and Fatima S., 2023. In: *INTER-NOISE and NOISE-CON Congress and Conference Proceedings,* **265,** 4055-4060. DOI: 10.3397/IN_2022_0578.

[39] Raj M., Fatima S. and Tandon N., 2021. *Green Mater,* **9,** 11-20. DOI: 10.1680/jgrma.19.00077.

[40] Standard Test Methods for Density and Specific Gravity (Relative Density) of Plastics by Displacement, 2020. https://www.astm.org/d0792-20.html (accessed July 31, 2022).

[41] Marathe U.N. and Bijwe J., 2020. *Wear,* pp. 446-447. 203189. DOI: 10.1016/j.wear.2020.203189.

[42] Standard Test Method for Tensile Properties of Plastics, 2022. https://www.astm.org/d0638-14.html (accessed December 31, 2022).

[43] Sayem A.S.M., Haider J. and Sayeed M.A., 2020. *J Compos Mater,* **54,** 1831-1845. DOI: 10.1177/0021998319885440.

[44] Standard Test Method for Measuring Vibration-Damping Properties of Materials, 2017. https://www.astm.org/e0756-05r17.html (accessed July 31, 2022).

[45] Standard Test Method for Normal Incidence Determination of Porous Material Acoustical Properties Based on the Transfer Matrix Method, 2019. https://www.astm.org/Standards/E2611.htm (accessed August 31, 2021).

[46] Ramos-De Valle L.F., 2013. In: Handbook of Polymer Synthesis, Characterization, and Processing, *John Wiley & Sons, Inc., Hoboken, NJ, USA,* pp. 451-461. DOI: 10.1002/9781118480793.ch23.

[47] Gowariker V.R., Viswanathan N.V. and Sreedhar J., 2022. In: 4th ed., *New Age International (P) Ltd., Delhi,* pp. 131-145.

[48] Rajesh M., Pitchaimani J., 2017. *J Bionic Eng,* **14,** 141-150. DOI: 10.1016/S1672-6529(16)60385-2.

[49] Mago J., Sunali, Negi A., S. Fatima, 2023. In: INTER-NOISE and NOISE-CON Congress and Conference Proceedings, **265,** 3549-3558. DOI: 10.3397/IN_2022_0501.

[50] Foulk J.A., Chao W.Y., Akin D.E., Dodd R.B. and Layton P.A., 2006. *J Polym Environ,* **14,** 15-25. DOI: 10.1007/s10924-005-8703-1.

[51] Rahman M.Z., Jayaraman K. and Mace B.R., 2017. *Fibers and Polymers,* **18,** 2187-2195. DOI: 10.1007/s12221-017-7418-y.

[52] Rahman M.Z., Jayaraman K. and Mace B.R., 2018. *Fibers and Polymers,* **19,** 375-382. DOI: 10.1007/s12221-018-7588-7.

[53] de Rosa S., Capobianco M., Nappo G. and Pagnozzi G., 2014. *Proc Inst Mech Eng C J Mech Eng Sci,* **228,** 3343-3355. DOI: 10.1177/0954406214530597.

[54] D'Alessandro V., Petrone G., Franco F. and de Rosa S., 2013. *Journal of Sandwich Structures & Materials,* **15,** 541-582. DOI: 10.1177/1099636213490588.

[55] Isaac C.W., Pawelczyk M., Wrona S., 2020. *Applied Sciences,* **10,** 1543. DOI: 10.3390/app10041543.

The Journal of Acoustical Society of India : Vol. 51, No. 1, 2024 (pp. 27-33)

Predicting the effect of hearing loss on distortion product otoacoustic emissions in humans

Naman Agarwal[1,2] and Sripriya Ramamoorthy[1*]

[1]Department of Mechanical Engineering, IIT Bombay, Mumbai-400 076, India

[2]Mechanical Cluster, UPES Dehradun, Dehradun-248 007 India

e-mail: ramamoor@iitb.ac.in

[Received: 06-02-2023; Revised: 11-12-2023; Accepted: 19-09-2024]

ABSTRACT

Distortion product otoacoustic emission (DPOAE) is used as a non-invasive tool to diagnose human hearing. In DPOAE, the cubic distortion tone emission is measured at the ear canal, which is generated due to the intermodulation of two tones (f_1 and f_2) in the cochlea at different stimulus levels. The DPOAE is measured with either varying primary frequency ratio (f_2/f_1), keeping one primary frequency constant at the same stimulus level, or varying stimulus level keeping the primary frequency ratio consistent. The DPOAE response of healthy cochlea is found to be bell-shaped with a 35-45 dB lower level compared to the primary stimulus level. This study considers a nonlinear mechano-electro-acoustic model for human cochlea to evaluate the DPOAE. The model contains two fluid-filled ducts coupled with Basilar Membrane (BM) and includes outer hair cell somatic feedback motility and nonlinear hair bundles mechano-electrical-transduction. The model is benchmarked with the BM response in human cadavers. The characteristics of DPOAE are predicted in the normal and impaired cochlea. The comparisons of normal and impaired ear DPOAE response help to describe the changes in response resulting from hearing loss in the human cochlea.

1. INTRODUCTION

Nonlinear compressive growth of sound-generated response with stimulus level is a characteristic of healthy mammalian cochleae[1] and forms the basis for the generation of distortion products (DPs)[1]. The intermodulation of sound-generated responses inside the cochlea due to two tones (f_1 and f_2) generates acoustic distortion products measured in the ear canal of animals and humans. Of these, the cubic DPOAE at the frequency ($2f_1$- f_2) is the strongest[2]. DPOAEs in humans have been measured for a wide range of stimulus frequencies and levels[2,3]. DPOAE level had a band-pass filtering characteristic observed in humans and rodents[2,3,4] when the frequency of one primary tone was fixed, and the other was swept[3,4]. DPOAE is a robust phenomenon routinely used for clinical purposes[4]. Several properties of DPOAE have been studied extensively in animals[2,5] and humans[3,4] that are at least qualitatively similar to the invasive measurement of animals[6].

It has been demonstrated in rodents that furosemide reduces the endocochlear potential, thereby hindering the power supply for outer hair cell (OHC) electromotility[7]. As a result, the auditory sensitivity is decreased by furosemide, and the basilar membrane (BM) input-output function at the characteristic

frequency loses its compressive nonlinearity and becomes linear with respect to the stimulus level[7]. The alteration of cochlear response due to the furosemide is similar to the response pattern observed with other permanent cochlear impairments[6]. Damage to the OHC causes several changes to auditory function[7]. As the generation of DPOAE depends on the integrity of the OHC electromotility, the responses are also reduced with hearing loss[6]. So, DPOAE is used as a non-invasive tool to detect impaired auditory function in humans[4].

In summary, the direct measurement of BM response as well as the indirect measurement in the form of DPOAE response in mammals can both reveal impairment in cochlear function. DPOAE tests are noninvasive and frequently used to detect hearing loss of cochlear origin, because direct measurements of the BM response in humans are currently not possible[3-4]. The similarities between direct cochlear response measures from lower animals and DPOAE measurements in humans and animals could provide insights into cochlear function over a wide range of levels and frequencies[6].

The present study aims to examine the characteristics of the DPOAE using a nonlinear human mechano-electro-acoustic (MEA) model[8,9] to infer cochlear response properties for both normal and impaired ears. Comparing normal and impaired ear[6] DPOAE responses helps describe the consequences of hearing loss in humans. DPOAEs for a wide range of primary levels and primary frequencies are simulated, and the results are compared with the data reported by Gaskill and Brown (1990)[3], Abadala (1996)[4]. The nonlinear MEA model of the human cochlea adapts our prior linear MEA model of the guinea pig cochlea[8,9] to humans and includes the nonlinearity due to mechano-electrical transduction in hair bundles[10]. Inspired by O'Connor and Puria (2008)[11], the transmission line human middle ear model is also integrated with the nonlinear MEA model[10]. The integration of middle ear model is needed to directly provide pressure input at the ear canal and to estimate DPOAE as the pressure at the ear canal.

2. MATERIAL AND METHODS

2.1 Middle ear integrated nonlinear MEA Model

In this study, a nonlinear MEA model of the human cochlea (Fig. 1)[8,9] is developed and integrated with transmission line middle ear model[11]. This physiologically motivated finite element model of human cochlea consists of three physical domains (mechanical, electrical, and acoustical domain), integrated along with their coupling terms. For more details, see[8,9]. The model includes three structural degrees of freedom at each cross-section: BM, HB, and OHC. Nonlinearities are incorporated into the model in the HB mechano-electrical transduction current (MET current) which is modelled by a first-order Boltzmann nonlinear function[12].

$$I_{hb} = G_a^{\max}(P_0 - P_0^s)\Delta V_{hb} \tag{1}$$

Where $G_a^{\max}$ is the maximum saturating HB mechano-electric conductance, ΔV_{hb} is the resting value of the difference between SM potential and intercellular OHC potential,

$$P_0 = \frac{1}{1+\exp\left(\frac{X_0 - u_{hb}}{\Delta X}\right)} \tag{2}$$

$P_0^S = 0.4$ is the resting open probability of the MET channel, X_0 at P_0^S and $\Delta X = \frac{K_b T}{f_{gs\gamma}}$ are displacement constants, K_b is the Boltzmann constant, T is temperature in kelvin, f_{gs} is the single channel gating force, and γ is the geometrical gain factor (relating the displacement in the HB tip link). The nonlinear governing equations of cochlear dynamics are discretized using Bubnov-Galerkin FE method and solved alternate time-frequency method[10].

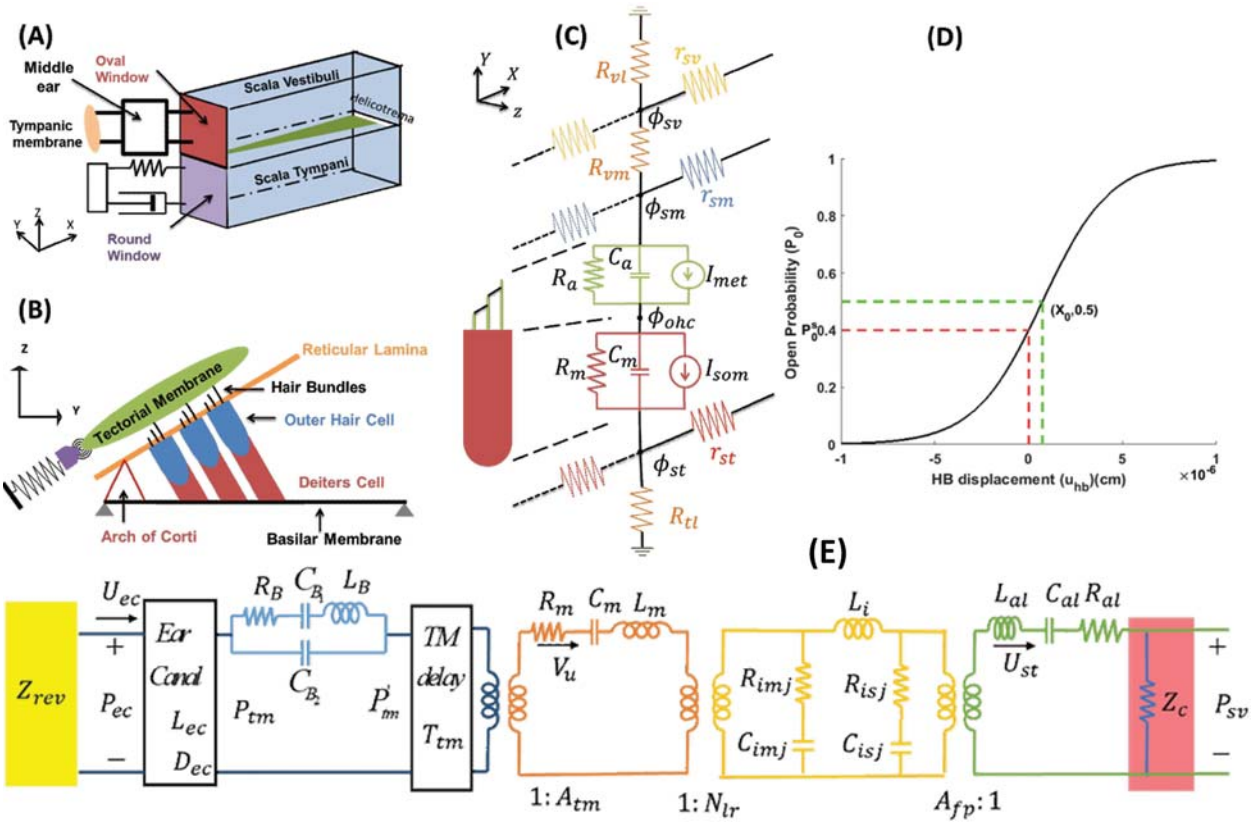

Fig. 1. Nonlinear MEA model of the cochlea[8,9]. (A) Fluid model. (B) Micromechanical model for the OoC structures. (C) Electrical network at given cross section of cochlea. I_{met} and I_{som} are the current sources due to HB conductance and OHC electromotility respectively. For more details see Agarwal and Ramamoorthy (2020)[9] (D) Nonlinear function in MEA model as first-order Boltzmann nonlinear probability function. Open probability of MET channel P_0 (function of HB displacement u_{hb}) is modeled as a Boltzmann first order function. (E) Transmission line human middle ear model, inspired by O'Connor and Puria (2008)[11]. Z_C is mainly due to the acoustic input resistance of the cochlea. Z_{rev} is reverse impedance at ear canal when sound is emitted from the cochlea to ear canal. P_{ec} and P_{sv} are the ear canal pressure and SV pressure, respectively.

$$\begin{bmatrix} K_f & Q_{fs} & 0 \\ Q_{sf} & K_s & Q_{se} \\ 0 & Q_{es}^{Lin} & K_e \end{bmatrix} \begin{pmatrix} p_m \\ u_m \\ \phi_m \end{pmatrix} + \begin{bmatrix} 0 \\ 0 \\ NL_m(u) \end{bmatrix} = \begin{pmatrix} f_m \\ 0 \\ 0 \end{pmatrix} \tag{3}$$

The quantities K_f, K_s and K_e are the stiffness terms of the fluid, the micromechanical structure, and the electrical degrees of freedom, respectively. Q_{sf} and Q_{fs} are from structure-fluid coupling at the BM. Q_{se} and Q_{es} represent the structural - electrical coupling at the OHC. NL_M is the nonlinear force vector due to the MET current. f_m is the forcing term on the fluid due to stapes, which is attached to the middle ear model, adopted from O'Conner *et al.* (2008)[11] (shown in Fig. 1 (E)). m is the index to map the frequency components. To determine the nodal value of fluid pressure, p_m structure displacement u_m, and electrical potential ϕ_m.

In the transmission line human middle ear model, as shown in Fig. 1 (E), the cochlear input impedance acts as the load which is computed using the ratio of the predicted SV pressure output relative to stapes

volume velocity input for forward wave propagation. In the reverse direction (for DPOAE predictions), rigid termination is assumed at the end of the ear canal, mimicking experimental conditions used for validation. The forward pressure transfer function (ratio of SV pressure to ear canal input pressure) and the reverse pressure transfer function (ratio of pressure at ear canal to SV pressure) have been validated with available experimental data for humans[14,15].

3. RESULTS AND DISCUSSIONS

The middle ear attached human nonlinear MEA model, discussed in the METHODS section, is used to predict the BM and OoC displacements, fluid pressures, cochlear microphonic potentials, and the middle ear responses, to sound input at the ear canal. DPOAE is predicted as the ear canal pressure resulting from the propagation of DP from the cochlea to the ear canal via the middle ear. Both pure tone, as well as two-tone stimuli, are considered as discussed next.

The variation of normalized BM response at 5 kHz best place relative to stapes, as a function of the stimulus frequency for different sound pressure levels is shown in Fig. 2 (A) and (B). At low sound pressure

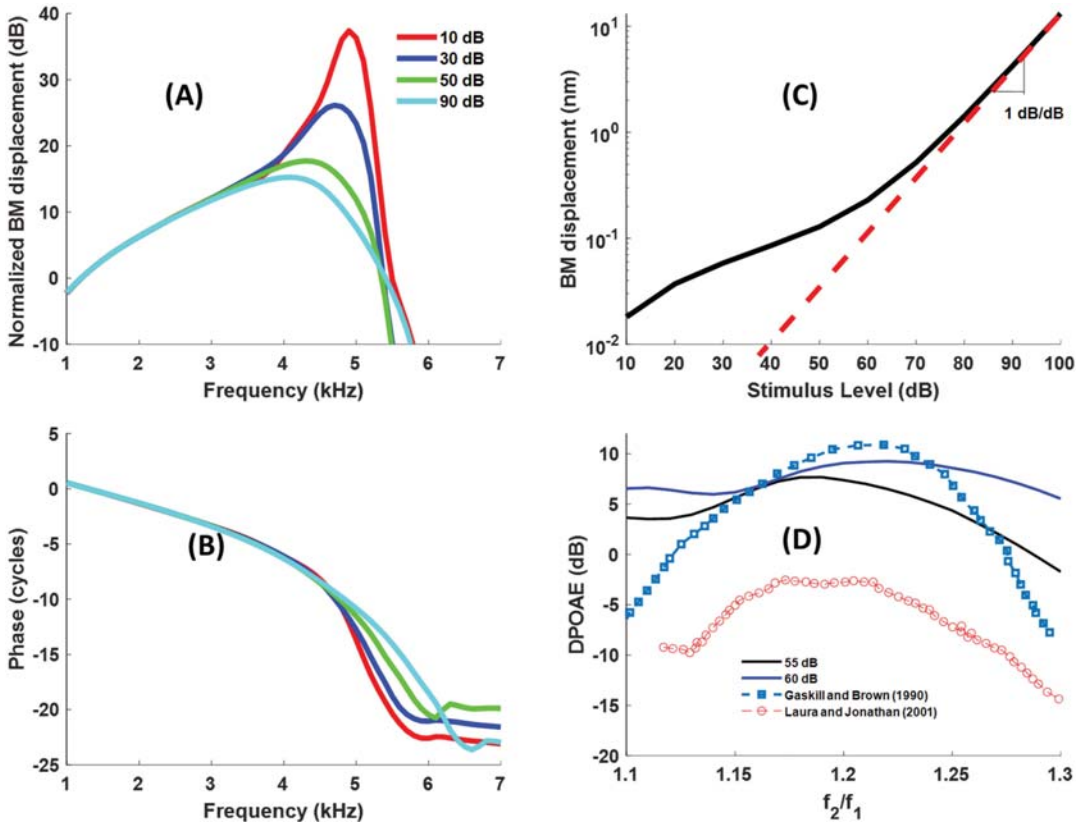

Fig. 2. (A) Magnitude and (B) phase of normalized BM re stapes displacement versus frequency at 5 kHz best place. (C) Input-output function of the nonlinear MEA cochlea model. At low stimulus level up to 25 dB and higher stimulus level from 70 dB the response shows linear with 1 dB/dB slope. The BM response is compressed with increasing stimulus levels and reaches passive response at high stimulus levels. (D) Cubic DPOAE estimated from MEA model at three different stimulus level ((L_1=L_2 =55,60 dB) for 5 kHz. The DPOAE response peaks around 1.2 to 1.22 and decreases with increasing frequency ratio, as expected from Gaskill and Brown 1990[3] and Laura and Jonathan (2001)[13].

levels, the normalized BM response curves have a steep high-frequency slope close to the CF and are narrowly tuned; at high sound pressure levels, the peak response shifts toward lower frequencies and the responses become broadly tuned. As frequency increases, BM phase responses to tones show lagging, as described in[1,8,9,10]. A clear shallow section at low frequency and a steep segment at a frequency about CF are present in the phase curve (Fig. 2(B))[1]. The BM magnitude and its phase are insensitive to alteration of ear canal pressure at frequencies lower than CF, which is consistent with experimental observation of other animals[1,8]. At CF, the BM gain is higher at low intensity than at high intensity, indicative of a compressive nonlinearity[1].

The nonlinear human MEA cochlear model predicts a compressive nonlinearity at CF, as also observed in other mammals[1]. The BM response is linear at very low intensity (up to about 20 dB SPL at ear drum) and at very high intensity (more than 100 dB SPL at ear drum). The compressive nonlinear curve slope at low stimulus level and high stimulus level is 1 dB / dB, similar to that observed in guinea pig experiments[1]. The passive BM response is found to be linear with respect to stimulus intensity as shown in Fig. 2 (C) .

The level of $2f_1$ - f_2 cubic DPOAE at the ear canal (see Fig. 2 (D)) is predicted as a function of the stimulus frequency separation (ratio = f_2/f_1) using the human nonlinear MEA model. In each simulation sequence with a constant f_1 frequency and variable f_2 frequency, the ratio was increased from 1.1 to 1.35 in 0.01 increments. The stapes displacement is predicted at the DP frequency and converted into ear canal pressure using the reverse middle ear path (refer to Fig. 1(E)). The effect of frequency separation is estimated at three different stimulus levels, keeping equal values for both tones, that is, L_1=L_2. The DPOAE response increases with frequency separation until an optimum f_2/f_1. Beyond that value, the response level declines with further increase in f_2/f_1[4,16,17]. In this simulation, the primary frequency f_1 is taken to be 5 kHz with variable f_2/f_1 for 55 and 60 dB SPL input at the ear canal. Figure 2 (D) shows that the optimum ratio lies between 1.15 to 1.2 for all three different SPL, similar to human DPOAE measurements shown in Gaskill and Brown 1990[3] and Laura and Jonathan (2001)[13]. At the optimum f_2/f_1, the predicted cubic DPOAE level is 50 dB below the level of the primaries, similar to experimental observations[3,4,16]. From the literature, it may be noted that the optimal ratio changes from subject to subject, as well as with age. For neonates, the ratio could vary from 1.2 to 1.23, while for adult subjects, it could vary from 1.18 to 1.2[4,17].

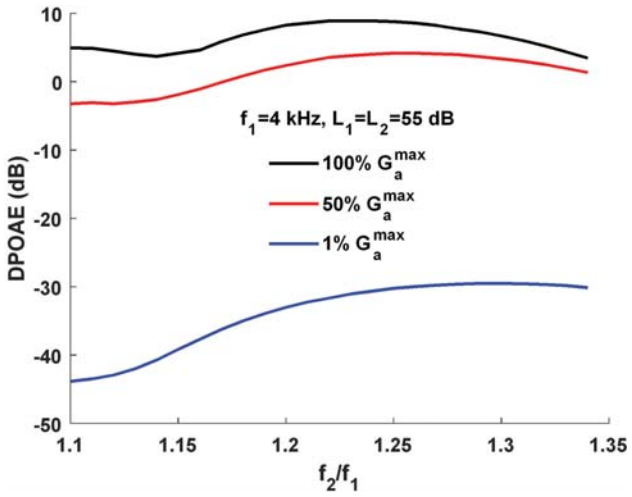

Fig. 3. Cubic DPOAE ($2f_1$-f_2) estimation from nonlinear MEA model of human cochlea. The response is shown for the case where one primary frequency is held constant while varying the primary frequency ratio for equal stimulus levels of primaries (L_1=L_2=55dB). The response is shown for three different health conditions of the cochlea. The cubic DPOAE level decreases by about 10 dB when the active feedback gain is reduced to half. And, when the gain is reduced to 1% (very low level of activity), the DPOAE level reduces by about 40-50 dB.

The sharpness of OoC response reduces with decreasing the activity feedback gain see Fig. 2 (A) and (B). Decreasing the active feedback gain indicates that loss in activity of hearing performance. In this simulation, the active feedback gain is reduced 50% (partially damaged) and 1% (nearly full damaged) and compared with the fully active response. In healthy cochlea, the HB current saturates at low stimulus level while in damaged cochlea, the current saturates at a larger SPL. As Fig. 2 (C) shows the BM response at CF in low SPL increases with SPL level or the decreasing of activity level in HB conductance slope (see Fig. 1 (D)). Similarly, the cubic DPOAE level is also reduced with activity level. A partially damaged cochlea with 50% reduction in active feedback gain shows about 10 dB decrease in cubic DPOAE level. For significantly reduced active feedback gain (1% of maximum value), the cubic DPOAE reduces by about 50 dB. The estimation of DPOAE by mathematical modeling as shown in this study for different hearing conditions could be a useful tool for identifying the cause of hearing loss.

4. CONCLUSION

The primary objective of this study to examine the DPOAE using a physiology-based model of the human ear. A previously developed MEA model, by Ramamoorthy *et al.* (2007)[8] (also see[9]) for guinea pig), is integrated with MET transduction nonlinearity and transmission line middle ear model developed by O'connor and Puria (2008)[11]. The model parameters are modified for the human cochlea to predict sound-induced response within the hearing range (20 Hz to 20 kHz). The benchmarked model is used to predict the cubic DPOAE in humans, which agrees reasonably with measured DPOAE. The model could improve by better fitting of the human nonlinear MEA model parameters. Except for a few parameters taken from literature for human cochlea, most of the model parameters are extrapolated from guinea pig for the 20 Hz to 20 kHz frequency range using the tonotopic scaling principle[18]. Except for some difference in DPOAE responses, the model can currently predict the expected basic characteristics of cochlea (such as amplification at low stimulus levels, frequency selectivity, compressive nonlinearity) similar to other mammals[1].

The predicted normalized BM response relative to stapes peaks at CF for low stimulus levels and the peak frequency decreases with increasing stimulus level. At frequencies away from the CF, the response is almost independent of stimulus level. The cubic DPOAE (or the $2f_1 - f_2$ component) predicted for varying primary frequency ratio (f_2/f_1) demonstrates a band-pass shape with a maximum at $f_2/f_1 = 1.2$ for $f_1 = 5$ kHz. The model shows that the f_2/f_1 value at which DPOAE is maximum varies with f1. This trend is qualitatively similar to experimental observations[3,4,16,17] but differs in the quantitative value of the primary frequency ratio.

5. ACKNOWLEDGEMENT

This work was supported by the grant BT/PR40821/MED/32/760/2020 from the Department of Biotechnology (DBT), India.

6. REFERENCES

[1] Robles L., and Ruggero M.A., 2001. Mechanics of the mammalian cochlea. *Physiological reviews,* **81**(3), 1305-1352. https://doi.org/10.1152/physrev.2001.81.3.1305.

[2] Kemp D.T., 2002. Otoacoustic emissions, their origin in cochlear function, and use. *British medical bulletin,* **63**(1), 223-241. https://doi.org/10.1093/bmb/63.1.223.

[3] Gaskill S.A. and Brown A.M., 1990. The behavior of the acoustic distortion product, $2f_1–f_2$, from the human ear and its relation to auditory sensitivity. *The Journal of the Acoustical Society of America,* **88**(2), 821-839. https://doi.org/10.1121/1.399732.

[4] Abdala C., 1996. Distortion product otoacoustic emission ($2f_1–f_2$) amplitude as a function of f_2/f_1 frequency ratio and primary tone level separation in human adults and neonates. *The Journal*

of the Acoustical Society of America, **100**(6), 3726-3740. https://doi.org/10.1121/1.417234.

[5] Magnan P., Avan P., Dancer A., Smurzynski J. and Probst R., 1997. Reverse middle-ear transfer function in the guinea pig measured with cubic difference tones. *Hearing research,* **107**(1-2), 41-45. https://doi.org/10.1016/S0378-5955(97)00015-4.

[6] Neely S.T., Johnson T.A., Kopun J., Dierking D.M. and Gorga M.P., 2009. Distortion-product otoacoustic emission input/output characteristics in normal-hearing and hearing-impaired human ears. *The Journal of the Acoustical Society of America,* **126**(2), 728-738. https://doi.org/10.1121/1.3158859.

[7] Frolenkov G.I., Belyantseva I.A., Kurc M., Mastroianni M.A. and Kachar B., 1998. Cochlear outer hair cell electromotility can provide force for both low and high intensity distortion product otoacoustic emissions. *Hearing research,* **126**(1-2), 67-74. https://doi.org/10.1016/S0378-5955(98)00150-6

[8] Ramamoorthy S., Deo N.V. and Grosh K., 2007. A mechano-electro-acoustical model for the cochlea: response to acoustic stimuli. *JASA,* **121**(5), 2758-2773. https://doi.org/10.1121/1.2713725.

[9] Agarwal N. and Ramamoorthy S., 2020. Balance in the feedback loop components of the mammalian cochlear amplifier. *JAP,* **128**(3), 034701. https://doi.org/10.1063/5.0010802.

[10] Meaud J. and Grosh K., 2012. Response to a pure tone in a nonlinear mechanical-electrical-acoustical model of the cochlea. *Biophysical Journal,* **102**(6), 1237-1246. https://doi.org/10.1016/j.bpj.2012.02.026.

[11] O'Connor K.N. and Puria S., 2008. Middle-ear circuit model parameters based on a population of human ears. *JASA,* **123**(1), 197-211. https://doi.org/10.1121/1.2817358.

[12] S.L. Johnson, M. Beurg, W. Marcotti and R. Fettiplace, 2011. "Prestin-driven cochlear amplification is not limited by the outer hair cell membrane time constant," *Neuron,* **70**(6), 1143-1154. https://doi.org/10.1016/j.neuron.2011.04.024.

[13] Dreisbach L.E. and Siegel J.H., 2001. Distortion-product otoacoustic emissions measured at high frequencies in humans. *The Journal of the Acoustical Society of America,* **110**(5), 2456-2469. https://doi.org/10.1121/1.1406497.

[14] Voss S.E., Rosowski J.J., Merchant S.N. and Peake W.T., 2000. Acoustic responses of the human middle ear. *Hearing research,* **150**(1-2), 43-69. https://doi.org/10.1016/S0378-5955(00)00177-5.

[15] Puria S., 2003. Measurements of human middle ear forward and reverse acoustics: implications for otoacoustic emissions. *The Journal of the Acoustical Society of America,* **113**(5), 2773-2789. https://doi.org/10.1121/1.1564018.

[16] Lasky R.E., 1998. Distortion product otoacoustic emissions in human newborns and adults. I. Frequency effects. *The Journal of the Acoustical Society of America,* **103**(2), 981-991. https://doi.org/10.1121/1.421215.

[17] Abdala C., 2000. Distortion product otoacoustic emission ($2f_1$-f_2) amplitude growth in human adults and neonates. *The Journal of the Acoustical Society of America,* **107**(1), 446-456. https://doi.org/10.1121/1.428315.

[18] Prodanovic S., Gracewski S.M. and Nam J.H., 2019. Power dissipation in the cochlea can enhance frequency selectivity. *Biophysical Journal,* **116**(7), 1362-1375. https://doi.org/10.1016/j.bpj.2019.02.022.

The Journal of Acoustical Society of India : Vol. 51, No. 1, 2024 (pp. 34-43)

Auditory filter shapes derived from psychophysical tuning curves

Dharmesh Verma[1], Preeti Rao[2] and Sripriya Ramamoorthy[3*]

[1]Centre for Research in Nanotechnology & Science,
Indian Institute of Technology Bombay, Mumbai, India
[2]Department of Electrical Engineering, Indian Institute of Technology Bombay, Mumbai, India
[3]Department of Mechanical Engineering, Indian Institute of Technology Bombay, Mumbai, India
e-mail: ramamoor@iitb.ac.in

[Received: 06-02-2023; Revised: 30-07-2024; Accepted: 16-09-2024]

ABSTRACT

Human hearing can be modelled with a set of auditory band-pass filters. Psychophysical tuning curves, obtained from simultaneous and forward masking-based measurements, are a powerful tool to derive the auditory band-pass filters for a given individual. An analysis of the tuning curve helps distinguish between normal and pathological impaired ears. The sharp selectivity of the narrow filters defines the sensitivity of the cochlea hearing. In this study, the frequency selectivity of the auditory system of the human subject is measured by masking a sinusoidal signal (0.5, 1.0, 2.0, 4.0 kHz) using both simultaneous and forward masking approaches. Preliminary results of the power spectrum, critical ratio, and auditory filter estimates are interpreted. The experimental results highlight the effects of the noise notch variations in the signal hearing levels.

1. INTRODUCTION

The human ear transduces sound stimuli into electrical signals that can be transmitted to the brain, where the perception of sound happens. Significant signal processing happens in the cochlea. The cochlea contains a basilar membrane that acts as a combination of auditory filter bands by vibrating at a particular place for a particular frequency. Specific locations of the basilar membrane resonate at a particular frequency, leading to the spatial organization of the frequency selectivity along the membrane[1]. Hence the auditory filters are associated with different points on the basilar membrane (position-frequency mapping). The auditory filters are theoretical / mathematical representations of the frequency selectivity of the auditory system. Hence, modelling auditory filters is crucial in analyzing the spectrotemporal analysis of sounds. These sets of filters represent the ability of the human ear to perceive and differentiate between sounds.

Auditory filter banks are non-uniform bandpass filter banks designed to imitate the frequency resolution of human hearing. From the works and experiments by Patterson and other researchers, the auditory filters can be classified as the Set of overlapping bandpass filters whose bandwidth varies with frequency, as shown in figure 1. Each filter has a bandwidth called a Critical Band at a particular centre frequency. The bandwidth of the auditory filter increases as the centre frequency increases. The shape of

the filter is found to be asymmetrical about the centre frequency. The critical band gives a close approximation of the bandwidth of the filter. When the filter is assumed to be rectangular with the same power as that of noise and amplitude of the signal, the bandwidth of this filter is the Effective Rectangular Bandwidth (ERB).

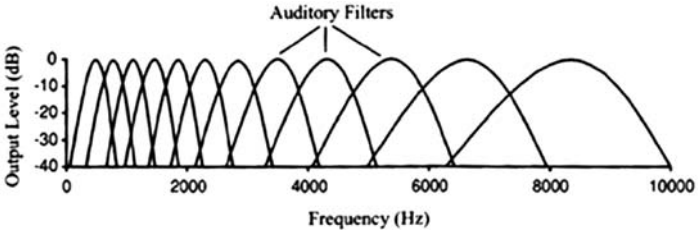

Fig. 1. Auditory Filter Bank[17].

The ERB increases with an increase in the centre frequency; hence the bandwidth of the auditory filters increases with an increase in the centre frequency. The ratio of signal power to noise power is known as the Critical Ratio, and it depends on the tone frequency and is a direct measure of the ERB. The measured thresholds are mathematically fitted to get the auditory filter. These models can be used to predict the filter behaviour for all the levels simultaneously. The auditory filters can be distinguished on the upper part and lower part consisting of "tip filter" and "tail filter" to indicate a sharp tip and broader tail appearance of the filter.

The auditory filter is estimated by varying the signal threshold with notch width and asymmetry[6], called iso-stimulus curves. In these experiments, the level of the noise masker is kept constant, and the signal threshold is varied. Generally, the signal frequency is kept close to the centre frequency. Major noise components which are outside the filter are rejected. The noise which passes through acts as a signal masker (dB SPL / Hz). This signal masker determines the level of the noise and affects the level of the signal threshold.[12,13]. This also results in calculations of the signal-to-noise of the auditory filter for a given bandwidth. Patterson & Moore (1986) named this phenomenon the 'power spectrum model' of masking. Notched noise is very similar to a band-stop filter and can be defined as noise that has a notch around the signal frequency that the subject is trying to detect in a certain bandwidth. The notched noise has the advantage of minimizing the signal-to-noise ratio improvement that can be achieved by shifting the filter[8,9,13]. This method uses spectral notches to calculate thresholds for detecting sinusoidal signals in noise as a function of notch width and position relative to the signal frequency. Patterson (1976) used a schematic illustration, as shown in Figure 2. The threshold of a sinusoidal signal is measured as a function of the spectral width. The spectral width is measured as the opening of the spectral notch in the noise masker. The amount of noise that passes through the auditory filter centred on the signal frequency is proportional to the shaded area. For notch noise, the signal threshold decreases with increasing notch width and *vice-versa.*

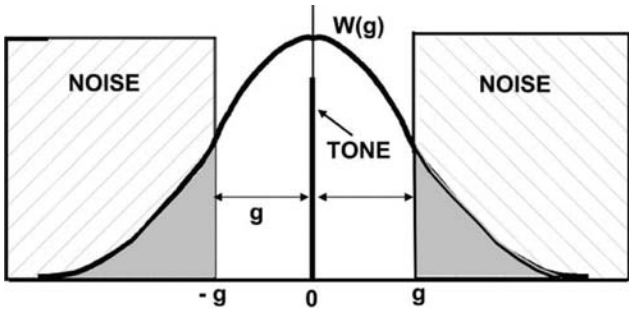

Fig. 2. Schematic representation of auditory filter with notch noise masking. The shaded area represents the effective noise that masks the tone[2].

Psychoacoustic Tuning Curves are used to measure auditory filters' frequency selectivity. The sharpness of frequency tuning in mammals, including humans, can be determined by PTCs. These psychological curves show the relationship between the sound SPL and the pure tone frequency masker required to just mask the sound. In the PTC test method, the signal level and centre frequency are kept at a constant level, usually a very low SPL and the noise masker level (dB SPL / Hz) is varied. This experimental approach wherein the signal level is kept constant, and the masker level is varied with notch variation is also named as Iso-Response stimuli experiment. The resulting curves are PTCs, representing the masker level needed at the input to just masking a tone signal. The increase in the notch opening results in a higher masker level required just to mask the signal level. Subject testing determines the masker level that masks the tone to various masker frequencies. PTCs represent the highest response of the auditory nerve fibre[9,10]. PTC quantifies the ability of frequency selectivity[7]. Hence, PTCs can be obtained by changing the signal level and masker level parameters[11].

The threshold is determined by the amount of noise passing through the filter. The threshold corresponds to the signal-to-noise ratio at the output of the filter[3]. Fletcher simplified the filters as flat top, rectangular with critical bandwidth CB. When the noise bandwidth increases, more noise passes through the filter, increasing the threshold. When the noise bandwidth reaches the filter bandwidth, the threshold ceases to increase and becomes constant. The bandwidth at which the threshold does not increase with the noise bandwidth is known as the critical bandwidth of the filter. The CB can be indirectly estimated by measuring the power of sinusoidal signal Ps required for detection in the white noise of power density No. If the signal-to-noise ratio is K (to be estimated), the CB is given by:

$$CB = \frac{Ps}{N_o K} \tag{1}$$

Fletcher estimated K=1.

The shape of the auditory filter can be estimated by :

$$P_s = K\int_{-\infty}^{\infty} N(f)\left|H(f)\right|^2 df \frac{Ps}{N_o K} \tag{2}$$

where the masker is represented by N (f) and the auditory filter by H (f), and Ps is the signal power at the threshold[2,3,4,5]. Roy Patterson devised a new method of masking. Here, the signal is fixed in frequency (f_o), and the masker is a noise with a bandstop. The threshold corresponds to a constant signal-to-masker ratio at the output of the filter[2]. Patterson implemented the notch noise masker. In the ideal noise notch bandstop approach, we can write equation 2 as :

$$P_s = K\int_{-\infty}^{-\Delta f / f_0} N(f)\left|H(f)\right|^2 df + KNf_0\int_{\Delta f / f_0}^{\infty}\left|H(f)\right|^2 \tag{3}$$

where Δf is the distance between the tone and the edge of the noise[2].

If the filter is symmetric, the above equation becomes

$$P_s = 2KN_0 f_0\int_{\Delta f / f_0}^{\infty}\left|H(f)\right|^2 df \tag{4}$$

Patterson simplified the equation as :

$$P_s = KN_0 f_0\int_{-\infty}^{\Delta f / f_0}\left|H(f)\right|^2 df \tag{5}$$

The derivative of Equation 5 with respect to $\Delta f/f_o$ can be given by:

$$\frac{dP_s}{d(\Delta f / f_0)} = KN_0 f_0\left|H\frac{\Delta f}{f_0}\right|^2 \tag{6}$$

The filter shape is given by the derivative of the threshold curve divided by the KN_0f_0 constant. An analytical expression for the shape of the auditory filter can be produced by fitting a polynomial to the set of tone thresholds and taking its derivative.

2. TEST PROCEDURE

The human subject testing reported in this study has been approved by the Institute Ethics Committee at the Indian Institute of Technology Bombay.

Human subject testing determines the masker level that simply masks the tone to various masker frequencies. A narrow band noise masker is allowed to pass around its centre frequencies, and the level at which sound is just masked is recorded. These resulting curves are PTC curves which represent the masker level needed at the input just to mask a tone signal.

Threshold measurements require highly specialised test equipment and an acoustic chamber. an acoustic chamber providing up to 20 dB of noise isolation is used to perform the subject testing. The human subject under test is requested to sit in the chamber as shown in Figure 3. A circumaural headphone (Sennheiser® make HD 559 Headphone) that covers the pinna and external ears is used on the human subject for the PTC measurements. The usage of circumaural headphones provides not only good fidelity of signal but also helps in additional external noise isolation. To generate the required noise notch algorithm Lab-View® software of NI (National Instruments®) is used. The PCI-6351® National Instruments driver card is plugged into the desktop PC to generate the required signal tone frequency and noise waveforms. This PCI 62351® board has two analog outputs with DACs of 16-bit and four analog inputs of 16-bit ADCs. The NI-AIO BNC 2110® box is used as an interface board, as shown in Figure 3. The signal and noise waveforms are generated as the analog output from the BNC 2110®. This signal gets connected to circumaural headphones (Sennheiser® make HD 559). The signal from the source is connected to the headphones via the use of a coaxial cable and BNC connectors. Initially, pure tones of a specific frequency and amplitudes are delivered to one ear at a time. The human subject is asked to signal with a 'thumbs up' for hearing the sound and a 'thumbs down' for not hearing anything.

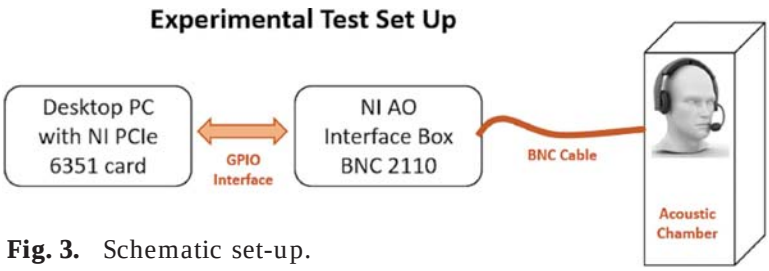

Fig. 3. Schematic set-up.

3. SUBJECTS

An audiogram is performed initially at all the standard audiometric frequencies on ten subjects, and their absolute threshold is found to be better than equal to 10 dB HL at 500 Hz, 1000 Hz, 2000 Hz and 4000 Hz as shown in figure 4. The age of the subjects is in the range of 20 to 30 years. Each subject was given a prior trial of practice after which their readings were recorded.

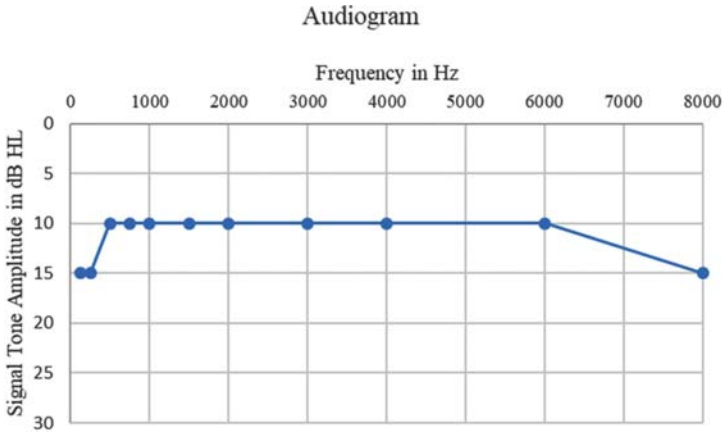

Fig. 4. Audiogram of one of the subjects

4. STIMULI

The level of the noise masker required just to mask the tone signal fixed in frequency and level is determined as a function of masker frequency using a two-interval forced-choice technique, suggested by Blackwell (1953). Generally, the masker is a narrow-band noise with a fluctuating centre frequency, while the target is a fixed frequency and fixed level pure tone at around 10 to 20 dB HL. The subject is asked to indicate which interval contained the more extreme stimulus, and performance is again summarised in terms of the proportion of correct responses[14]. The observation interval of the subject is recorded. The step size is 5 dB up to the first four turns and reduced to 2 dB later. Three trials were performed for each test procedure, and a mean threshold is tabulated. The notch width is represented as the ratio to the centre frequency, symmetrically placed around the fc as $\Delta f / fc$ (also mentioned by variable 'g' by various researchers). This ratio is varied for five conditions 0, 0.1, 0.2, 0.3 and 0.4 for each frequency of operation. Tuning Curves where a sinusoidal or a narrow band noise masker is swept across its centre frequencies and the level at which sound is just masked is recorded.

5. SIMULTANEOUS MASKING

Here, the tone signal and the masker signal are played simultaneously to the subject. The signal (dB SPL) is a 50 ms raised cosine with 25 ms rise and 25 ms off and no flat portion. The masker level (dB SPL / Hz) is 200 ms with 25 ms onset and offset timing[15].

6. FORWARD MASKING

The masker signal appears first, followed by the tone signal to the subject. The signal (dB SPL) is a 25 ms raised cosine with 12.5 ms rise and 12.5 ms off and no flat portion. The masker level (dB SPL / Hz) is 200 ms with 25 ms onset and offset timing. A delay of 500 ms is added after each sequence[15]. The stimulus was presented monaurally to each ear.

7. METHOD TO MEASURE THE THRESHOLD

In the notched-noise method, the subject is presented with a notched noise as the masker and a sinusoid (pure tone) as the signal. The notched noise is noise with a notch around the frequency of the signal the subject is trying to detect and contains noise within a certain bandwidth. Notched noise is used as a masker to prevent the subject from hearing beats of a pure sinusoidal tone. The tests can be performed in two ways. First, by keeping the tone amplitude constant and changing the amplitude of the noise signal. The minimum signal amplitude threshold, which the human subject can hear, is measured. Second by keeping the noise amplitude constant and changing the amplitude of the tone signal. The minimum noise amplitude threshold required to mask the signal tone by which the human subject is not able to hear the tone is measured.

In the iso-response test performed, the second option is chosen, wherein the noise level is kept constant at 40 dB SPL / Hz. The signal thresholds are calculated through simultaneous masking when the signal is played to the subject simultaneously as the noise masker. The notched opening of the masker frequency varies from 0.1 to 0.9 times in the steps of 0.1 and the readings are taken, keeping the tone frequency constant. This measurement takes a considerable amount of time, around 30 to 45 minutes. The same test is performed three times on the subject, and the mean value is tabulated.

8. RESULTS

The mean masked threshold of the subject in simultaneous masking for iso-tuning curves is obtained by keeping the noise masker level fixed at 40 dB SPL / Hz. The obtained pattern is similar across all the subjects, as shown in Figure 5.

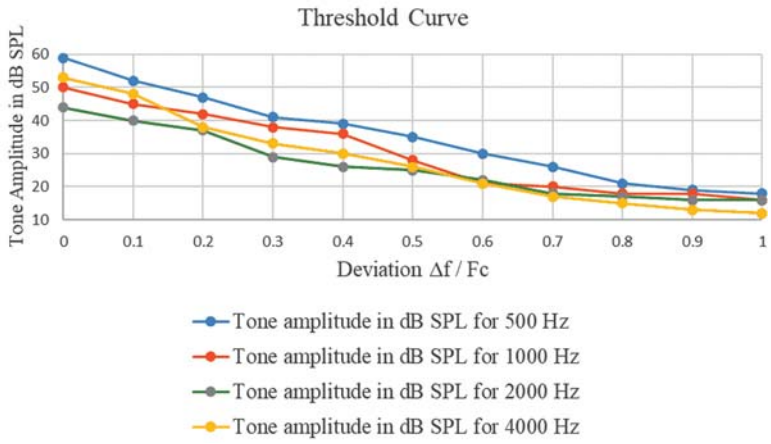

Fig. 5. Mean masked thresholds in dB SPL are obtained at 500 Hz, 1000 Hz, 2000 Hz and 4000 Hz in noise notch simultaneous masking with masker level at 40 dB SPL / Hz.

The abscissa represents the deviation of the notch variation implemented symmetrically towards both sides of the notch masker.

The verification of the above experimentally collected data is benchmarked with the results of Brian Glasberg and Brian Moore[16], as shown in figure 6. The obtained results show that as the notch width increases, the signal level (dB) reduces.

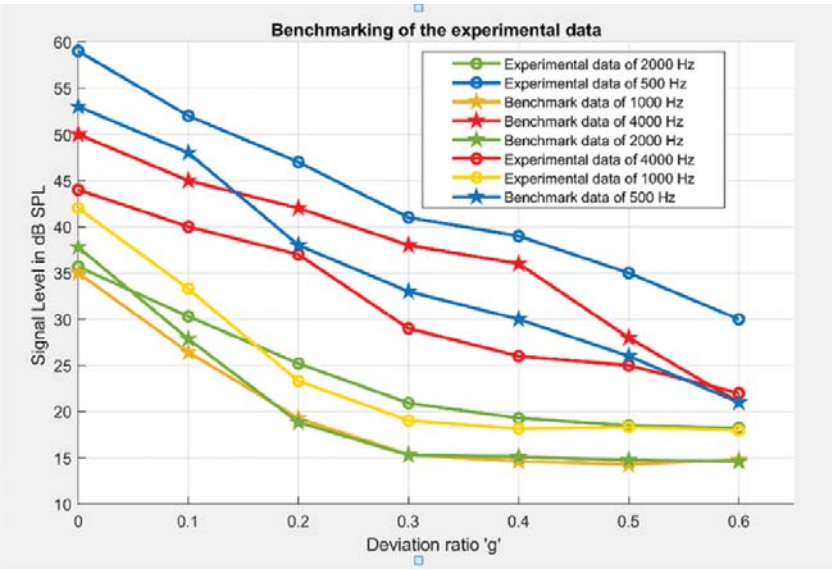

Fig. 6. Benchmarking of the experimental data with reference data of Brian Glasberg and Brian Moore[16].

According to Patterson and Nimmo-Smith (1980), this threshold curve implies that the auditory filter behaves like a pair of back-to-back exponentials with a rounded top instead of a sharp one and shallow skirts beyond f / fo = 0.4[18].

To define the filter, a mathematical model in MATLAB is created as a simplified version of their rounded-exponential filter. The threshold values obtained experimentally are fitted at 500Hz, 1000Hz, 2000Hz and 4000 Hz, as shown in figure 7.

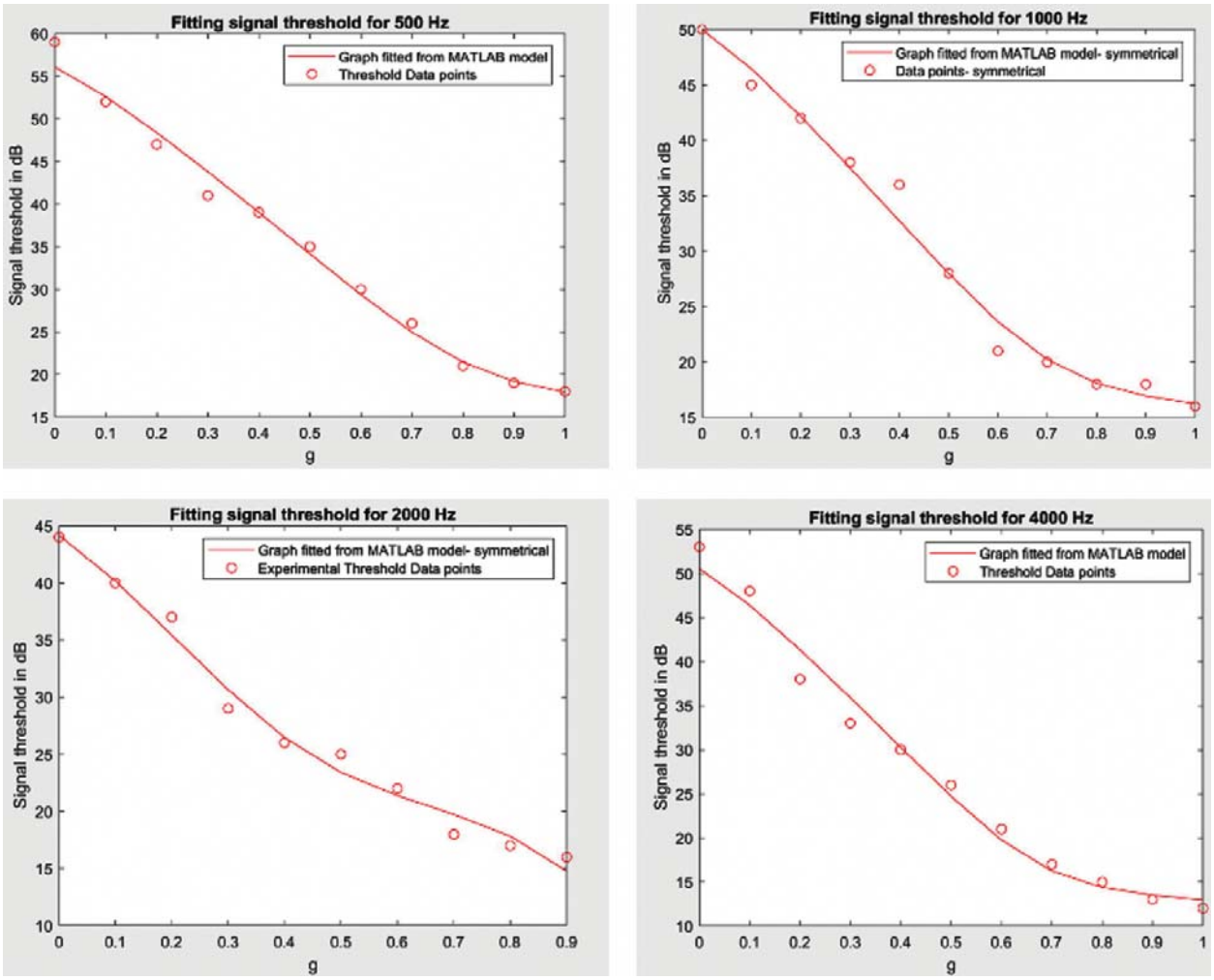

Fig. 7. Polyfit plot of the threshold curve plot at 500 Hz, 1000 Hz, 2000 Hz and 4000 Hz.

Using the proposed simple, poly-fit approach of the rounded exponential roex(p,r) model by Patterson (1976), the primary filter shapes are derived at different frequencies. Figure 8 shows the simplified filter patterns obtained by the Matlab model at various frequencies of 500 Hz, 1000 Hz, 2000 Hz, and 4000 Hz. The model does not include any corrections pertaining to the cochlea gain factor. The gain at the centre frequency is assumed to be zero and the attenuation at other frequencies is expressed relative to this. Each obtained auditory filter function provided suitable fits to the respective data.

For a linear system, the filter's gain is assumed to be absent. Both the upper and lower parts include parameters that define their slopes. Here we plotted symmetrical filters without the physiological (cochlea) gain factor. Ideally, the filters are asymmetric. The auditory filters can be distinguished on the upper part and lower part consisting of a "tip filter" and "tail filter" to indicate a sharp tip and broader tail appearance of the filter.

ERBs can be derived further from each filter plot, and the experiment may be repeated with different masker levels as proposed by researchers to study masker level dependency.

The mean masked threshold of the subject in forward masking for iso response threshold curves is obtained by keeping the signal level fixed at 20 dB SPL and varying the noise masker level. The threshold

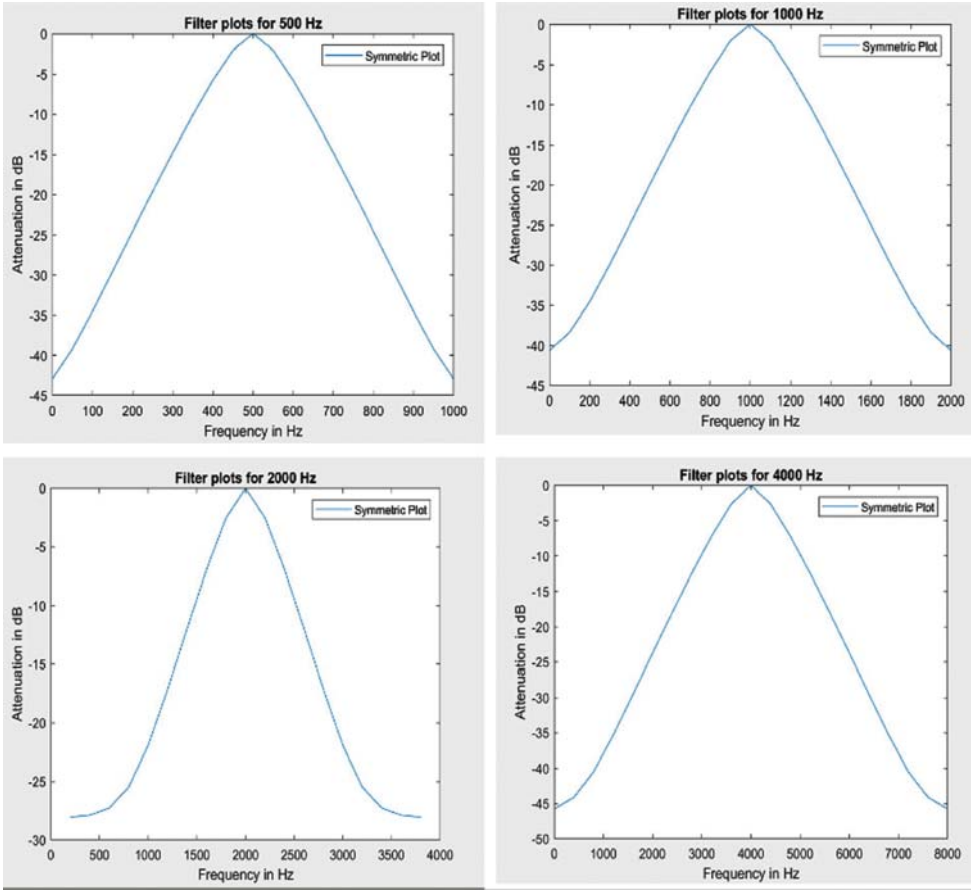

Fig. 8. Auditory Filter shape derived from the mean masked data at centre frequencies of 500 Hz, 1000 Hz, 2000 Hz and 4000 Hz.

values of the masker level in figure 9 indicate that as the notch width increases, the masker level (dB) increases.

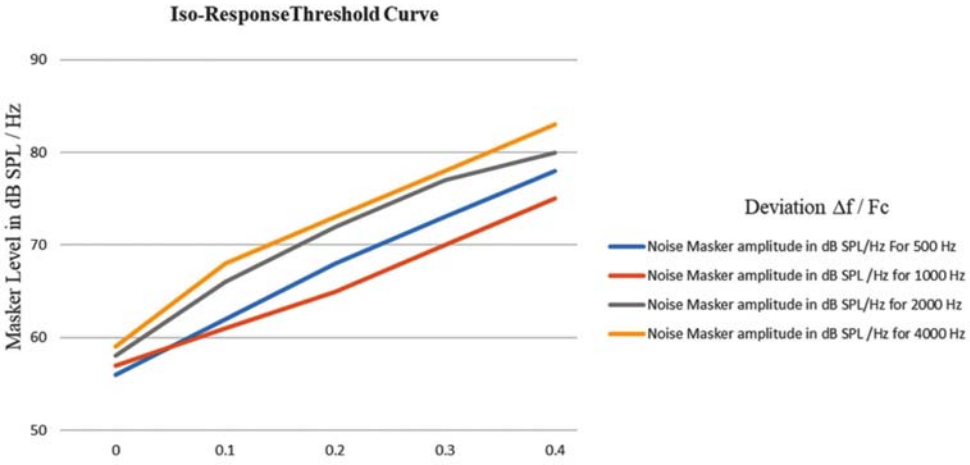

Fig. 9. Mean masked iso response thresholds obtained in the forward masking with noise notch masker. Benchmarking of the experimental data with reference data[14].

The results show that as the notch width increases, the masker level has to be higher to mask the signal level (dB).

The verification of the above experimentally collected data is benchmarked with the results of Unoki and Tan[14] and is shown in figure 10.

The experiment may be repeated with different signal levels to study signal level dependency.

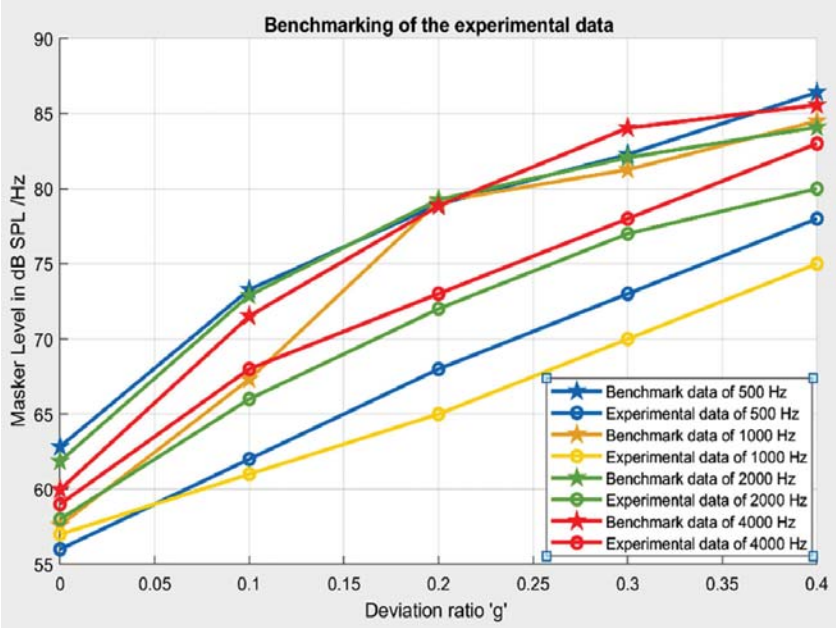

Fig. 10. Benchmarking of the experimental data with reference data[14].

9. SUMMARY

The frequency tuning and selectivity of the normal listener is very sharp compared to a physically impaired person whose shape of the auditory filter lacks sharpness and selectivity. Impaired listeners are found to have broader auditory filter responses, hence less frequency selectivity. This paper describes the methodology to perform the iso-stimulus tests required to generate an auditory filter bank and iso-response test necessary to generate the psychophysical tuning curves of the human subject. Here, we successfully conducted experiments based on signal level dependency and masker level dependency with two approaches to masking, simultaneous masking and forward masking. The noise notch data (in a symmetric masker approach) for individual subjects is fitted with a basic filter shape without a physiological gain factor. The resultant plots of the experimental data show the same trendlines as in benchmark reference data and validate our approach to experimentation. We plan to enhance the proposed models in future and use them to predict the normal hearing of different signal subjects.

The future work comprises estimating the auditory filter shapes with gain estimation, which can be modelled using both forward and simultaneous masking. This information will help in estimating the sharpness and frequency selectivity of the hearing of the human subject and will help in distinguishing normal and impaired listeners.

10. ACKNOWLEDGEMENT

This work was supported by the grant BT/PR40821/MED/32/760/2020 from the Department of Biotechnology (DBT), India.

11. REFERENCES

[1] Munkong R. and Juang B.H., 2008. Auditory perception and cognition. *IEEE Signal Processing Magazine,* **25**(3), 98-117.

[2] Goldstein E.B., 2010. Sound, the auditory system, and pitch perception. *Sensation and Perception,* pp. 259-289.

[3] Robles L. and Ruggero M.A., 2001. Mechanics of the mammalian cochlea. *Physiological reviews,* **81**(3), 1305-1352.

[4] Ruggero M.A., Rich N.C., Recio A., Narayan S.S. and Robles L., 1997. Basilar-membrane responses to tones at the base of the chinchilla cochlea. *The Journal of the Acoustical Society of America,* **101**(4), 2151-2163.

[5] Cooper N.P. and Rhode W.S., 1997. Mechanical responses to two-tone distortion products in the apical and basal turns of the mammalian cochlea. *Journal of Neurophysiology,* **78**(1), 261-270.

[6] Baker R.J. and Rosen S., 2006. Auditory filter nonlinearity across frequency using simultaneous notched-noise masking. *The Journal of the Acoustical Society of America,* **119**(1), 454-462.

[7] Moore B.C., 1995. Frequency analysis and masking. *Hearing,* **161,** 205.

[8] Goldstein E.B., 2010. *Sensation and Perception,* p. 490.

[9] Zwicker E., 1974. On a psychoacoustical equivalent of tuning curves. In Facts and Models in hearing. *Springer, Berlin, Heidelberg,* pp. 132-141.

[10] Shabana M., Moore B.C., El-Khosht M., Selim M.H. and Dokla M., 2014. Fast psychophysical tuning curves of the cochlea in normal-hearing individuals. *Advanced Arab Academy of Audio-Vestibulogy Journal,* **1**(1), 12.

[11] Zwicker E. and Schorn K., 1978. Psychoacoustical tuning curves in audiology. *Audiology,* **17**(2), 120-140.

[12] Glasberg B.R. and Moore B.C., 1990. Derivation of auditory filter shapes from notched-noise data. *Hearing Research,* **47**(1-2), 103-138.

[13] Patterson R.D., 1976. Auditory filter shapes are derived from noise stimuli. *The Journal of the Acoustical Society of America,* **59**(3), 640-654.

[14] Unoki M., Ito K., Ishimoto Y. and Tan C.T., 2006. Estimate of auditory filter shape using notched-noise masking for various signal frequencies. *Acoustical science and technology,* **27**(1), 1-11.

[15] Leschke J., Orellana G.R., Shera C.A. and Oxenham A.J., 2022. Auditory filter shapes derived from forward and simultaneous masking at low frequencies: Implications for human cochlear tuning. *Hearing Research,* **420,** 108500

[16] Glasberg Brian R. and Brian C.J. Moore, 2000. "Frequency selectivity as a function of level and frequency measured with uniformly exciting notched noise." *The Journal of the Acoustical Society of America,* **108**(5), 2318-2328.

[17] Moore B.C., 1995. Frequency analysis and masking. *Hearing,* **161,** 205.

[18] Patterson R.D., Nimmo-Smith I., Weber D.L. and Milroy R., 1982. The deterioration of hearing with age: Frequency selectivity, the critical ratio, the audiogram, and speech threshold. *The Journal of the Acoustical Society of America,* **72**(6), 1788-1803.

The Journal of Acoustical Society of India : Vol. 51, No. 1, 2024 (pp. 44-50)

Employing massive MIMO-OFDM technique in underwater acoustic communication

Shaik Azeez[1] and Bikramaditya Das[1,2*]

[1]Department of Electronics & Telecommunication Engineering, VSS University of Technology, Burla-768 018, Odisha, India

[2]Department of Electronics & Telecommunication Engineering, Biju Patnaik University of Technology, Rourkela-769 015, Odisha, India

e-mail: adibik09@gmail.com

[Received: 17-02-2023; Revised: 11-12-2023; Accepted: 13-09-2024]

ABSTRACT

UWAC is a method of conveying and getting information while submerged in water. There are several methods for identifying these linkages, but hydrophones are the standard in the great majority of cases. The UWAC is complicated in its presentation of multipath propagation, time-varying nature, and limited available transmission capacity. The growing requirement for transmission capability, spatially diversity, and UWAC performance has opened the way for the use of MIMO systems. MC modulation, such as OFDM, enables high-rate broadcast over long dispersive channels, whereas MIMO approaches boost total network capacity. The combination of MIMO with OFDM has shown to be a talented way out for a wide range of applications. However, modulation techniques must be adjusted dependent on underwater environmental factors such as temperature, salinity, depth, currents, waves, interference, and turbidity. This article investigates how the Web of Underwater Things (IoUT) might be used to differentiate improvements based on their degree of detail and overall performance. For feature analysis, a few modulation methods are used in the validation. The entire Underwater Wireless Communication (UWC) channel involves the creation and verification of receivers using MATLAB alongside the bellhop simulator software. This process assesses parameters such as the odds of error, s/n value, p_e of identification.

1. INTRODUCTION

UWAC is experiencing a growing demand for various applications. The selection of techniques and development models is enhancing the data transmission, spatial diversity, and efficiency of Underwater Wireless Communication (UWC). Electromagnetic, radiofrequency, and optical waves experience limited propagation in seawater, resulting in a significant reduction in signal strength. To address this, a channel estimation algorithm in the angle domain and frequency-selective, designed specifically for the MIMO model, has been proposed[1]. This algorithm is divided into two stages. In the initial step, non-zero tap positions are identified, and in the subsequent stage, point space coefficients are recognized. This model effectively evaluates the frequency-selective channel to reduce the complexity of Underwater Wireless

Communication (UWC). Recent research on various UWC assessment methods, such as pilot-based, least square (LS), and small minimum mean square error (MMSE) models, is examined, leading to the identification of potential future approaches for channel estimation. The cumulative probability proportion indicators validate the occurrence of errors attributed to time variations in the channel[2]. Over the past two decades, experts have continually enhanced both bit error rates and data rates. OFDM serves as an alternative approach to single-carrier modulation, swiftly addressing inter-symbol interference due to its resilience against multipath effects. The seamless integration of the MIMO model enhances the functionality of the complex equalizer.

Multipath communication degrades channel efficiency compared to single-carrier transmission. To address these challenges, MIMO-OFDM approaches are implemented across all channels in underwater communication systems. By employing frequency-trusted communication procedures, underwater acoustic communication and its information rates have seen improvement. The implementation of various phase shift keying systems, in particular, enhances signal-to-noise ratio and overall performance. In this study, the bit error rate was determined as 100 bps for MFSK-FH, validating the enhanced bandwidth efficiency of the underwater mode[4].

A communication method resistant to multipath effects and utilizing orthogonal chirp multiplexing technology has been developed. This approach enhances robustness, homogeneity, and blurring parameters. Simulation results demonstrate superior performance in terms of bit error rate and multipath resistance. The OFDM model, known for its high robustness in multipath communication for Underwater Wireless Communication (UWC), is employed. Gatekeeper spans effectively address inter-carrier interference during transmission, making this work particularly suitable for underwater channel estimation to eliminate gaps in UWC[5]. This design effectively minimizes end-to-end delay without any energy consumption. It also addresses issues related to low transmission, signal-to-noise ratio, and delays in Underwater Wireless Communication (UWC)[6]. The construction of underwater acoustic networks is based on a constraint model. Due to significant attenuation in water, radio waves and optical waves are heavily weakened, making acoustic signals the standard choice for UWC. Environmental factors directly impact the speed of sound waves, and incorrect acoustic signals can lead to mispositioning outcomes. Therefore, least square error and balance correction methods are implemented to mitigate the uncertainty of acoustic signals. The applied symmetry correction and constraint algorithm demonstrate excellent performance, remaining insensitive to the speed of an acoustic signal[7,8].

2. PROBLEM STATEMENT

The Cracken result representation is utilized to assess channel responses for the selected examination. The sea depth ranges from one meter to 10 meters, and the choice of transducers spans from 1 to n, depending on the application. The distance between the hydrophone and the n-transducer varies from 100 meters to 1000 meters. Communication between the m^{th} antenna and the n^{th} hydro receiver can be cross-checked. The simulator offers options such as multipath selection, where 2 to 10 multipaths are chosen for operational assessment. The primary channel delay is anticipated to be 15 ms, and the standard additional channel is selected for both present and expectations examinations.

2.1 Outlook method of UWAC

Massive MIMO-OFDM technologies are required to develop an efficient underwater communication system. These models become more efficient by employing various optimization strategies.

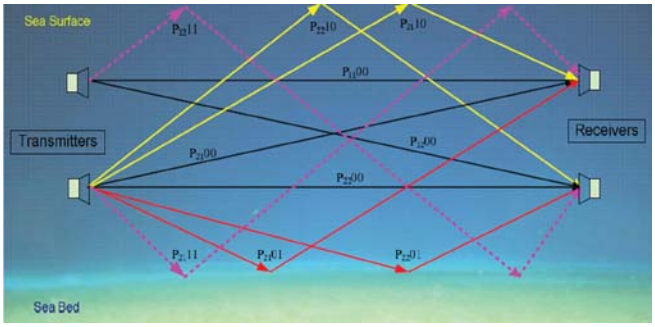

Fig. 1. Underwater multiple pathways channel impact.

Communication in the process to assessing the UWC channel For the ideal outcome, the Doppler scaling coefficient has been identified. D_p = Drake scaling factor θ_p = angle of impact at particular acoustic signal[18].

$$D_p = \left(\frac{v_r}{c}\right)\cos\theta_p \tag{1}$$

In above equation 1, the TX/RX velocity can be conveyed by the Doppler shift velocity of the transmitter or receiver, 'c' representing the speed of the acoustic wave in water. In general, the 'c' in UWC is high V_r, which makes the D_p essentially non-existent. A number of paths of communication was developed based on theoretical and experimental calculations.This has an influence on D_p for several carriers, resulting in inter-carrier interference. Acoustic signals are degraded by the UWC spectrum.OFDM techniques for reducing PAPR based on pre-coding selective connecting and false intervals were offered.

3. PROPOSED METHOD

The non-linear UWC spectrum falls in acoustic signal performance. OFDM were available for diminishing PAPR through pre-coding discriminatory mapping and forged intervals.

m^{th} antenna and the n^{th} hydro receiver comprise the advanced massive MIMO-OFDM paradigm. The time duration has represented as. $S_k = S_c + L/t$

$$L = -L/2 \ldots\ldots L/2\text{-}1 \tag{2}$$

Where SC embodies carrier frequency, SK specifies Support carrier frequency, and 1/t signifies subcarrier spacing. L signifies the number of subcarriers, while B denotes the bandwidth. P(T) = pulse shaping filter, Eu(k) = encrypted data symbol. Compute the Nth transducer transmitted signal using these figures

$$\tilde{x}N(t) = 2\mathrm{Re}\left\{\left[\sum_{k\varepsilon S_A} Sv,\ u[K]e^{j2\pi\frac{k}{T}t}\ p(t)\right]e^{j2\pi fct}\right\} \tag{3}$$

The transceiver couple for a multiway channel is formed up of S_v, and u avenues and the impulse response may be determined by combining these elements

$$h_{v,u}(\tau,t) = \sum_{p=1}^{pv,w} A_{v,u}\delta(\tau(\tau_{v,u} - D_p t)) \tag{4}$$

$A_{(v,u)}$ refers to the amplitude, $\tau_{(v,u)}$ is the time delay, and D_p is the Doppler shift factor. This mathematical computation precisely quantifies the impulse response of undersea communication's existing dynamic flavor. The output signal at the Vth receiver, in addition to noise acceptance, is provided by

$$\tilde{y}_{v(t)} = \sum_{u=1}^{Nt}\sum_{f=1}^{fv,w} A_{v,u,f}\tilde{x}_u(1 + a_{v,u,f})t - \tau_{v,u}) + \tilde{n}_v(t) \tag{5}$$

$$s_1(t) \approx R_C \sin(2\Pi f_c t)0 \le t \le T_b \tag{6}$$

$$s_0(t) \approx R_C \sin(2\Pi f_c t + \Pi)0 \le t \le T_b \tag{7}$$

The QPSK signal within a symbol duration Tb is defined as:

$$s_0(t) \approx R_C \sin(2\Pi f_c t + \Pi)0 \le t \le T_b \tag{8}$$

$$n = 1 \text{ to } 4$$

$$\theta_n = (2n-1)\Pi / 4$$

Where in the IQ plane, 8 Component-Shift Keying (8PSK) is a kind of segment modulation with eight phase states positioned in the IQ plane at 0, +/-(Pi/4), +/-(Pi/2), and +/-(Pi3/4) radians.

4. UWC MASSIVE MIMO HARDWARE DESIGN MODEL

The huge MIMO approach has advantages for UWC gearbox designs. The majority of the channel estimate is based on MIMO engineering.. However, in the great majority of circumstances, necessary innovations are required for UWC, procedures that have tremendous promise in communication innovation. The profound understanding might lead to the compelling concept that time and channel bounds must alter.

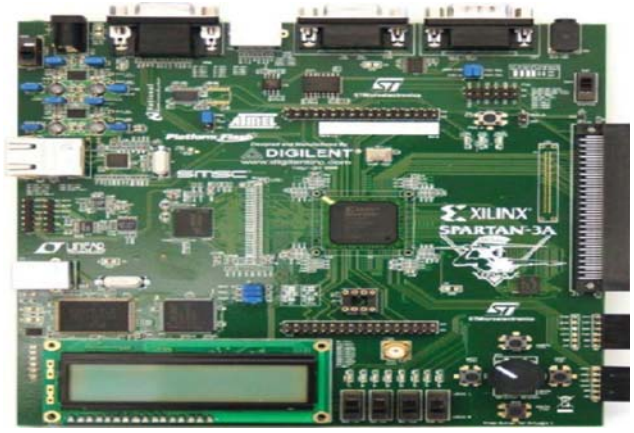

Fig. 2. FPGA device used at for the UWC project.

5. RESULTS

The overarching exploration successfully tackles the challenges inherent in general MIMO underwater communication, such as information rates. The accompanying elucidation emphasizes the UWAC has several advantages. The weighted Fourier partial frequency is suppressed in underwater acoustic communication channels. Communication via a single carrier is inefficient. The multi-carrier transmission and reception are established by the fractional Fourier change with crossover carrier communication. After the midway Fourier transform demodulation solutions, this novel design reduces intercarrier interference in UWC. Furthermore, for high SNR and information rates, the provided results beat UWC. The graph below depicts the oceanic square outline model as well as firm support.

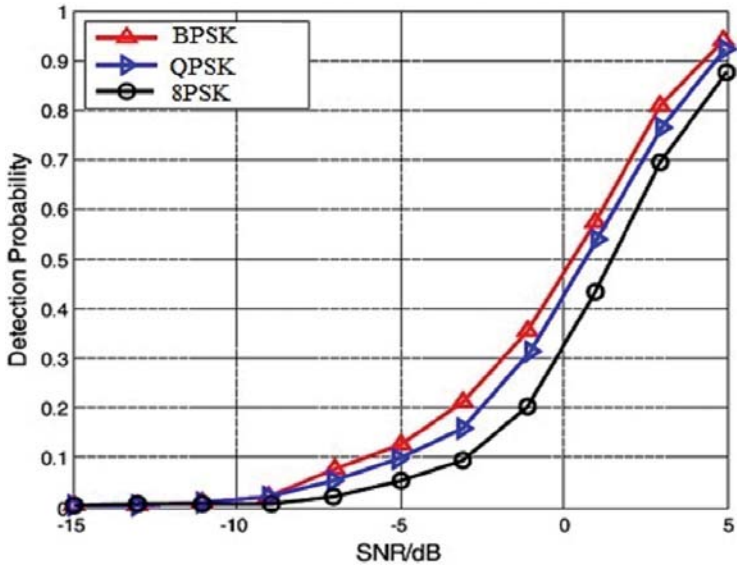

Fig. 3. Relationship of S / N to P_eD.

The epic techniques of range signal finding by underwater communication method provide the signal-to-noise proportion and PeD connections. Figure 5 shows that 8PSK outperforms QPSK and BPSK in terms of identification likelihood.

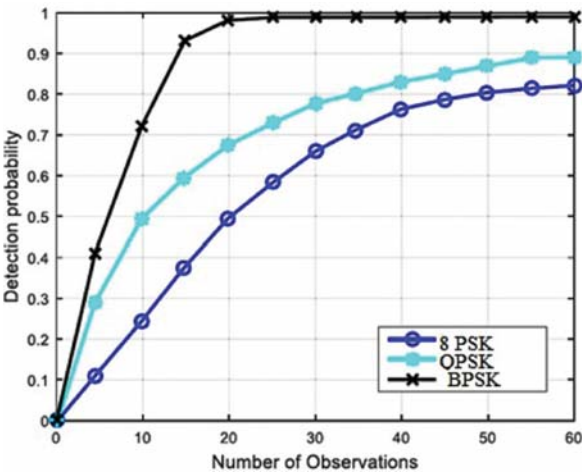

Fig. 4. No. Observation to P_eD.

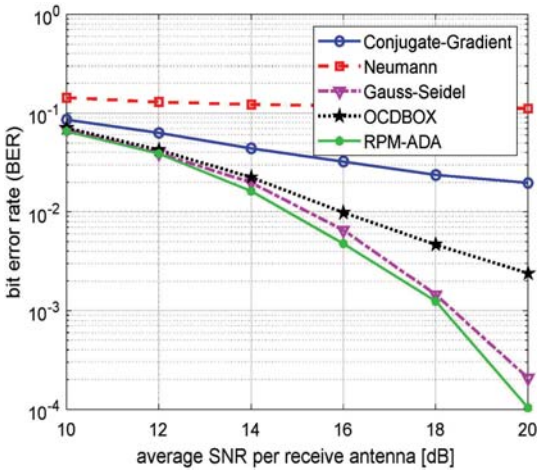

Fig. 5. BER to SNR transformation using an innovative channel model and an 8PSK modulation technique.

As a result, BER for UWC channels must be reduced such that the suggested framework performs better in temporal variation and low bandwidth instances. With the 8PSK modulation methodology, every in receipt of antenna interacted with several channels in the UWC.

The figure 6 shows that the number of user equipment per SE in this MMSE un-correlation error is greater than the DAMR correlation. Using this approach, the appropriate MMSE and MR signal for the UWC communication channel needs to be established.

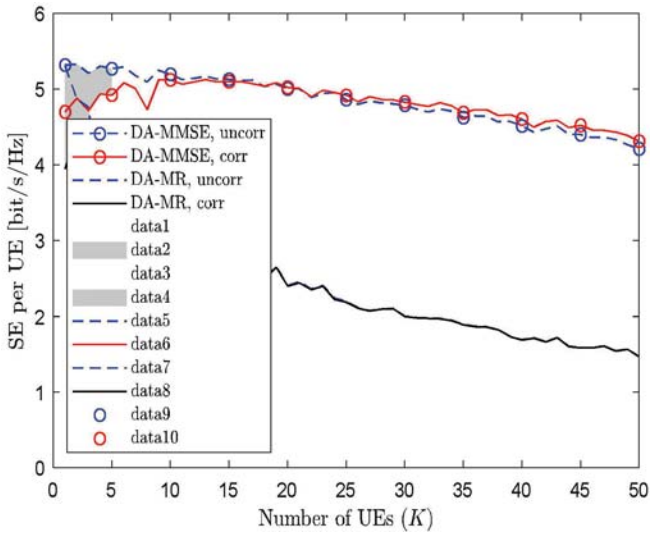

Fig. 6. MMSE and SE analysis.

6. CONCLUSION AND FUTURE WORK

In the current research, we examined and simulated several situations with varying depths, distances, and BER values using various underwater modulation schemes in order to demonstrate a relevant association between modulation systems. Our simulation findings show that the BPSK, QPSK and 8PSK approaches have higher BER, S/N ratio, and detection probability. As a result, using these strategies can

help to extend the life of an submarine design by improving dependability and efficiency. In UWC, the large MIMO design overcomes channel multipath and subcarrier struggles. System focused on huge MIMO-OFDM underwater acoustic communication employing the largest Mary PSK to increase SNR and bit error rate outcomes. MATLAB programming is used to view the simulation results.

7. ACKNOWLEDGEMENT

This work is supported by the Research Project Grant, OURIIP-2021 under Odisha State Higher Education Council (OSHEC), who have been supportive and worked actively to provide us with the protected academic time to pursue those goals.

8. REFERENCES

[1] B. Das and S. Das, 2009. "RAKE-MMSE Time Domain Equalizer for High Data Rate UWB Communication System," *Annual IEEE India Conference, Ahmedabad, India,* pp. 1-4, doi: 10.1109/INDCON.2009.5409346.

[2] M.R. Khan and B. Das, 2021. "Multiuser detection for MIMO-OFDM system in underwater communication using a hybrid binary spotted hyena optimizer", *Journal of Bionic Engineering,* **18,** 1-11.

[3] M.R. Khan, B. Das and B.B. Pati, 2020. "Channel estimation strategies for underwater acoustic (UWA) communication: An overview," *Journal of the Franklin Institute,* **357**(11), 7229-7265.

[4] M.R. Khan, S. Mahapatra and B. Das, 2020. "UWB Saleh-Valenzuela model for underwater acoustic sensor network," *International Journal of Information Technology*, **12**(4), 1073-1083.

[5] B. Das, S. Tiwari and S. Das, 2011. "Performance Study of Discrete Wavelet Packet Based MB-OFDM System for Short Range Indoor Wireless Environment," *International Conference on Devices and Communications (ICDeCom), Mesra, India,* pp. 1-5, doi: 10.1109/ICDECOM.2011.5738567.

[6] M.J. Bocus, A. Doufexi and D. Agrafiotis, 2016. "Performance evaluation of filter bank multicarrier systems in an underwater acoustic channel," *IEEE 27th Annual International Symposium on Personal, Indoor, and Mobile Radio Communications (PIMRC), Valencia, Spain,* pp. 1-6.

[7] D. Li-Da, W. Shi-Lian and Z. Wei, 2018. "Modulation Classification of Underwater Acoustic Communication Signals Based on Deep Learning", *OCEANS - MTS/IEEE Kobe Techno-Oceans (OTO), Kobe, Japan*, pp. 1-4,

[8] Chunguo Li, Kang Song and Luxi Yang, 2017. "Low computational complexity design over sparse channel estimator in underwater acoustic OFDM communication system" *IET Communications,* **11**(7), 1143-1151.

[9] K. Pelekanakis and L. Cazzanti, 2018. "On Adaptive Modulation for low SNR Underwater Acoustic Communications", *OCEANS 2018 MTS/IEEE Charleston, Charleston, SC, USA,* pp. 1-6.

[10] B. Lawal, S.S. A. Ali and A.B. Awang, 2010. "Massive MIMO systems for underwater acoustic communication," *IEEE International Conference on Underwater System Technology: Theory and Applications (USYS), Penang,* pp. 159-164.

[11] Das B., Subudhi B. and Pati B.B., 2016. Cooperative formation control of autonomous underwater vehicles: An overview. *Int. J. Autom. Comput.* **13,** 199-225.

[12] Mhd Tahssin Altabbaa, Erdal Panayirci, "Channel Estimation and Equalization Algorithm for OFDM-Based Underwater Acoustic Communications Systems",

[13] Kari D., 2017. "Robust adaptive algorithms for underwater acoustic channel estimation and their performance analysis. Digital Signal Processing", *International Conference on Wireless Communications, Networking and Mobile Computing,* pp. 57-68.

14. Sahoo S.P., Das B. and Pati B.B., 2021. Path Planning of Bio-inspired Swarm of AUVs using Distributed Path Consensus algorithm. *Journal of Engineering Science & Technology Review*, **14**(5), 173-178.

15. D.B. Kilfoyle, J.C. Preisig and A.B. Baggeroer, 2015. "Spatial Modulation Experiments in the Underwater Acoustic Channel", *IEEE Journal of Oceanic Engineering*, **30**(2), 406-415.

16. S. Roy, T.M. Duman, V. McDonald and J.G. Proakis, 2007. "High-Rate Communication for Underwater Acoustic Channels Using Multiple Transmitters and Space-Time Coding: Receiver Structures and Experimental Results", *IEEE Journal of Oceanic Engineering*, **32**(3), 663-688.

17. Sahoo S.P., Das B. and Pati B.B., 2022. Path Planning of AUV Swarms Using a Bio-inspired Multi-Agent System. *ECTI Transactions on Electrical Engineering, Electronics, and Communications*, **20**(3), 315-328.

INFORMATION FOR AUTHORS

ARTICLES

The Journal of Acoustical Society of India (JASI) is a refereed publication published quarterly by the Acoustical Society of India (ASI). JASI includes refereed articles, technical notes, letters-to-the-editor, book review and announcements of general interest to readers.

Articles may be theoretical or experimental in nature. But those which combine theoretical and experimental approaches to solve acoustics problems are particularly welcome. Technical notes, letters-to-the-editor and announcements may also be submitted. Articles must not have been published previously in other engineering or scientific journals. Articles in the following are particularly encouraged: applied acoustics, acoustical materials, active noise & vibration control, bioacoustics, communication acoustics including speech, computational acoustics, electro-acoustics and audio engineering, environmental acoustics, musical acoustics, non-linear acoustics, noise, physical acoustics, physiological and psychological acoustics, quieter technologies, room and building acoustics, structural acoustics and vibration, ultrasonics, underwater acoustics.

Authors whose articles are accepted for publication must transfer copyright of their articles to the ASI. This transfer involves publication only and does not in any way alter the author's traditional right regarding his/her articles.

PREPARATION OF MANUSCRIPTS

All manuscripts are refereed by at least two referees and are reviewed by the Publication Committee (all editors) before acceptance. Manuscripts of articles and technical notes should be submitted for review electronically to the Chief Editor by e-mail or by express mail on a disc. JASI maintains a high standard in the reviewing process and only accept papers of high quality. On acceptance, revised articles of all authors should be submitted to the Chief Editor by e-mail or by express mail.

Text of the manuscript should be double-spaced on A4 size paper, subdivided by main headings-typed in upper and lower case flush centre, with one line of space above and below and sub-headings within a section-typed in upper and lower case understood, flush left, followed by a period. Sub-sub headings should be italic. Articles should be written so that readers in different fields of acoustics can understand them easily. Manuscripts are only published if not normally exceeding twenty double-spaced text pages. If figures and illustrations are included then normally they should be restricted to no more than twelve-fifteen.

The first page of manuscripts should include on separate lines, the title of article, the names, of authors, affiliations and mailing addresses of authors in upper and lowers case. Do not include the author's title, position or degrees. Give an adequate post office address including pin or other postal code and the name of the city. An abstract of not more than 200 words should be included with each article. References should be numbered consecutively throughout the article with the number appearing as a superscript at the end of the sentence unless such placement causes ambiguity. The references should be grouped together, double spaced at the end of the article on a separate page. Footnotes are discouraged. Abbreviations and special terms must be defined if used.

EQUATIONS

Mathematical expressions should be typewritten as completely as possible. Equation should be numbered consecutively throughout the body of the article at the right hand margin in parentheses. Use letters and numbers for any equations in an appendix: Appendix A: (A1, (A2), etc. Equation numbers in the running text should be enclosed in parentheses, i.e., Eq. (1), Eqs. (1a) and (2a). Figures should be referred to as Fig. 1, Fig. 2, etc. Reference to table is in full: Table 1, Table 2, etc. Metric units should be used: the preferred from of metric unit is the System International (SI).

REFERENCES

The order and style of information differs slightly between periodical and book references and between published and unpublished references, depending on the available publication entries. A few examples are shown below.

Periodicals:

[1] S.R. Pride and M.W. Haartsen, 1996. Electroseismic wave properties, *J. Acoust. Soc. Am.*, **100** (3), 1301-1315.

[2] S.-H. Kim and I. Lee, 1996. Aeroelastic analysis of a flexible airfoil with free play non-linearity, *J. Sound Vib.*, **193** (4), 823-846.

Books:

[1] E.S. Skudzryk, 1968. *Simple and Comlex Vibratory Systems*, the Pennsylvania State University Press, London.

[2] E.H. Dowell, 1975. *Aeroelasticity of plates and shells*, Nordhoff, Leyden.

Others:

[1] J.N. Yang and A. Akbarpour, 1987. Technical Report NCEER-87-0007, Instantaneous Optimal Control Law For Tall Buildings Under Seismic Excitations.

SUMISSIONS

All materials from authors should be submitted in electronic form to the JASI Chief Editor: B. Chakraborty, CSIR - National Institute of Oceanography, Dona Paula, Goa-403 004, Tel: +91.832.2450.318, Fax: +91.832.2450.602,(e-mail: bishwajit@nio.org) For the item to be published in a given issue of a journal, the manuscript must reach the Chief Editor at least twelve week before the publication date.

SUMISSION OF ACCEPTED MANUSCRIPT

On acceptance, revised articles should be submitted in electronic form to the JASI Chief Editor (bishwajit@nio.org)